REVIEW

Microelectrode arrays based on carbon nanomaterials: emerging electrochemical sensors for biological and environmental applications

Rongsheng Chen,[a] Yong Li,[a] Kaifu Huo*[ab] and Paul K. Chu*[c]

We present an overview of the recent advances pertaining to microelectrode arrays (MEAs) constructed from carbon-based nanomaterials, especially aligned carbon nanotubes (CNTs) and carbon nanofibers (CNFs). The electrochemical and chemical activities of carbon nanomaterials depend on the microstructures, especially the graphitic edge plane sites. This review focuses on the electrochemical behavior associated with the microstructures and arrangement of the MEAs. Coupling plasma enhanced chemical vapor deposition (PECVD) with catalyst patterning techniques, low-density CNTs and individually addressable CNFs have been developed for multimode recordings with high temporal and spatial resolution. By introducing a nanowire core along the axis of CNFs to facilitate electron transfer, core–shell TiO_2/C and TiC/C nanofiber arrays have been fabricated and exhibit inner core-dependent electrochemical behaviors. The TiC/C nanofibers show excellent electrochemical behavior due to good electrical contact as well as the conducting nanowire core that offers an ideal transport pathway for electrons. Applications of carbon nanomaterials to electrochemical sensors, ranging from biomolecules to inorganic ions from biological and environmental samples, are discussed.
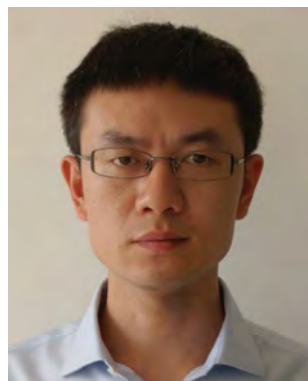
1. Introduction

Microelectrodes, defined as electrodes with at least one dimension smaller than the diffusion layer thickness of the electroactive species,[1] have received considerable attention since the pioneering investigations in the early 1980s.[2,3]

[a]*Wuhan University of Science and Technology, Wuhan 430081, China*
[b]*Wuhan National Laboratory for Optoelectronics, Huazhong University of Science and Technology, Wuhan 430074, China. E-mail: kfhuo@hust.edu.cn*
[c]*City University of Hong Kong, Hong Kong, China. E-mail: paul.chu@cityu.edu.hk*

Microelectrodes offer a number of advantages over their conventional counterparts such as fast establishment of a steady-state signal, decreased ohmic drop in potential and smaller double-layer capacitance.[4] These characteristics have created new possibilities for microelectrodes as electrochemical sensors in biological and environmental applications. For example, microelectrodes can be readily applied to probing of chemical events on the surface of tissues or individual biological cells with high spatial and temporal resolution due to their small size, fast response, and large signal-to-noise ratios.[5] The high rate of mass transport at the microelectrodes

Rongsheng Chen

Rongsheng Chen received his B.S. in Chemistry from Wuhan University in 1998 and Ph.D. in Analytical Chemistry from Wuhan University in 2005. He is currently an Associate Professor of College of Chemical Engineering and Technology at Wuhan University of Science and Technology. His research interests include electrochemical sensors, carbon nanomaterials, microfluidics and photocatalysis.

Yong Li

Yong Li received his B.S. in Material Science from Wuhan University of Science and Technology in 2011. He is currently a graduate student of School of Materials and Metallurgy at Wuhan University of Science and Technology. His research activity includes nanomaterials and electrochemical sensors.
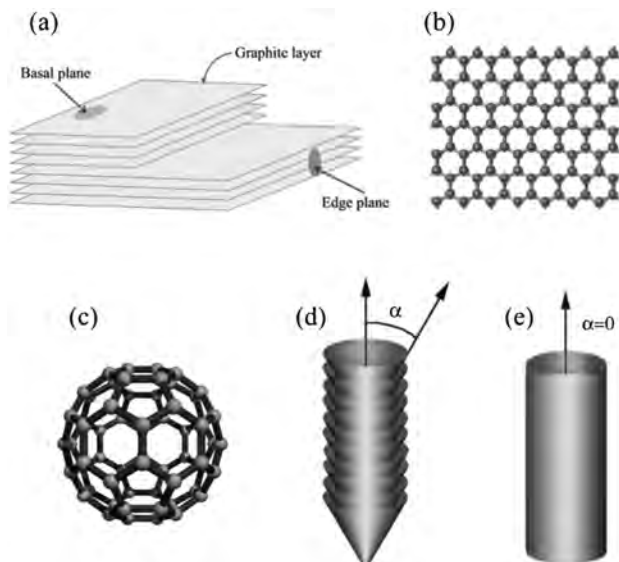
Fig. 1 Schematic structure carbon nanomaterials.: (a) A crystal of HOPG in which the layers of graphite have an interlayer spacing of 3.35 Å, (b) Graphene layer, (c) Fullerene, (d) Stacked cone herringboned nanofiber, and (e) Nanotube. (a) Reproduced from ref. 16 with permission from The Royal Society of Chemistry. (b)–(e) Reprinted with permission from ref. 17, copyright 2005 American Institute of Physics.

enables measurement of kinetics by steady-state methods rather than transient techniques. The improved diffusion characteristics of the microelectrodes allow measurements in static solutions with minimal perturbation of the system. Moreover, microelectrodes can also be applied to solutions with a very low concentration of analytes in a supporting electrolyte due to the reduced ohmic drop and capacitive effects.[6]

The electrical signal at a single microelectrode is often in the range of picoamperes to nanoamperes, and so a high precision potentiostat inside a well-designed Faraday cage is needed to minimize the electromagnetic interference from electronic devices in the vicinity. The experimental difficulties can be circumvented by utilizing microelectrode arrays (MEAs) typically consisting of tens to millions of microelectrodes. MEAs possess most of the advantages of microelectrodes and provide many orders of magnitude larger output current than a single microelectrode. On account of the excellent analytical performance, MEAs have been extensively explored to determine electroactive species such as neurotransmitter release from rat pheochromocytoma (PC12) cells,[7,8] oxygen and nitric oxide release from fibroblast cells,[9] heavy metal ions,[10] nucleic acids,[11] and hydrogen peroxide (H_2O_2).[12] The diffusion profile of the microelectrodes in the array is either independent of or overlaps on the experimental timescale according to the microelectrode size and space between each individual microelectrode.[13]

Carbon has long been the electrode material of choice due to its wide potential range, rich surface chemistry, minimal fouling, availability in a variety of forms, and low cost. The most ordered three dimensional (3D) carbon materials is highly ordered pyrolytic graphite (HOPG) which consists of layers of graphite parallel to the surface and with an interlayer spacing of 3.35 Å (Fig. 1a). The plane composed of sp^2-bonded hexagonal carbon atoms is known as the "basal plane", whereas the irregular surface perpendicular to the "basal plane" is known as the "edge plane". The edge and basal planes exhibit great differences in the chemical as well as electrochemical activities, and they are the fundamental issues in the electrochemical behavior of carbon electrodes.[14,15] The edge planes are more active than the basal planes. The heterogeneous charge transfer rate constants, k^0, at HOPG edge-planes are estimated to be $\sim 10^7$ times higher than those at basal-planes.[16] Graphene can be considered as a single layer of HOPG crystal and this 2D hexagonal honeycomb lattice of carbon atoms serves as the basic building block of graphite

Kaifu Huo received his B.S. in Applied Chemistry from China University of Petroleum in 1997 and Ph.D. in Physical Chemistry from Nanjing University in 2004. He is currently a full Professor of National Lab for Optoelectronics in Huazhong University of Science and Technology. He is an associate editor of Nanoscience and Nanotechnology Letters. He has authored/co-authored more than 90 papers in international refereed journals. His main research activities encompass nanobiomaterials and nanostructured electrode materials for electrochemical biosensor and energy storage devices including lithium-ion battery and supercapacitors.

Kaifu Huo

Paul K Chu received his PhD in chemistry from Cornell University and is presently Chair Professor of Materials Engineering in City University of Hong Kong. His research activities encompass plasma surface engineering and materials science. He is Chairman of the Plasma-Based Ion Implantation (PBII&D) International Committee, a member of the Ion Implantation Technology (IIT) International Committee and IEEE Nuclear and Plasma Science Society Fellow Evaluation Committee, senior editor of IEEE Transactions on Plasma Science, and associate editor of Materials Science & Engineering Reports. He is a Fellow of the APS, AVS, IEEE, MRS, and HKIE.

Paul K. Chu

and other carbon nanomaterials[17,18] such as 0D fullerenes, 1D carbon nanotubes (CNTs), and quasi-1D carbon nanofibers (CNFs) (Fig. 1b–e). The CNTs can be envisioned as a rolled-up seamless graphene tube with the pristine walls of a CNT being the graphitic basal planes and the tube ends as the graphitic edge planes (Fig. 1c). The graphene sheets in CNFs are not parallel to the axis and the edges of different graphene sheets end at the sidewalls (Fig. 1d), thus exhibiting improved electrochemical activity due to the high exposure of graphite edge-plane sites. In general, CNFs consist of curved graphene layers arranged as stacked cones, cups, or plates.[19,20] Nanostructured carbon electrodes, especially CNFs-based electrodes have a large surface area which is easily accessible by electroactive species in the solution and the high density of exposed edge planes yields high electrochemical activity, thus resulting in excellent analytical performance in a variety of applications.[21–27]

There has been an explosion of interest in recent years to develop MEAs based on highly oriented CNTs and CNFs.[11,28–30] Plasma-enhanced chemical vapor deposition (PECVD) has become the most frequently adopted approach to prepare these MEAs. The vertically aligned CNTs (VACNTs) or CNFs (VACNFs) on a conducting substrate offers the direct electrical connection between the MEAs and underlying collector. Coupling CVD synthesis with standard photolithography procedures allows patterned growth of VACNTs/VACNFs and these highly oriented MEAs can be synthesized at precisely defined locations with a wide range of size scales from nanoelectrodes to wafer-scale areas on the underlying supporting substrates.[31,32] The fabrication strategies can be further applied to prepare individually addressable MEAs that are well suited for high throughput screening pharmaceutical compounds as well as investigating electrochemical events with high temporal and spatial resolution, for instance, dynamic physiological processes from cellular communication.[8,33–36]

This paper will review the recent research activity on MEAs constructed by CNTs, CNFs, and core–shell structured CNFs. Emphasis is given to the electrochemical behavior associated with the microstructures and arrangement of the MEAs. The applications of electrochemical sensors based on carbon nanomaterials ranging from biomolecules, inorganic ions to biological and environmental samples are also discussed.

2. Carbon nanomaterials

2.1 Carbon nanotubes

CNTs can be categorized as single-walled nanotubes (SWNTs) and multi-walled carbon (MWNTs) according to the layers of rolled graphene sheets.[37] SWNTs comprise a single graphite sheet rolled with tube diameters of 1–2 nm, whereas MWNTs are concentric tubes of rolled-up graphene and separated by an interlayer distance close to that of graphite (0.34 nm). CNTs used to construct electrochemical sensors usually have lengths of micrometers to tens of micrometers, although ultralong CNTs over tens of centimeters long have been reported.[38] It

has been suggested that the electrocatalytic properties of CNTs with enhanced currents and reduced peak-to-peak separation (ΔE_p) in voltammetry can be attributed to the ''inherently unique'' properties of CNTs.[39–41] However, the detailed ''inherently unique'' properties affecting electrochemical biosensing properties are not involved.

On account of the anisotropic microstructure of CNTs, the electrochemical activity on the tube ends differ greatly from that on the sidewalls of the CNTs. The open tube ends of the CNTs are analogous to the HOPG edge planes, whereas the sidewalls are relatively inert and similar to those of basal planes of HOPG.[42] Compton and co-workers demonstrated the electrocatalytic properties of CNTs should be contributed by the tube ends via a comparison between the electrochemical oxidation of epinephrine and electrochemical reduction of ferricyanide at the CNTs modified electrodes.[43] Ajayan and co-workers showed the perfect Nernst behavior for electrochemical reactions of $Fe(CN)_6^{3-/4-}$ redox on a MWNTs microbundle electrode.[44] The ΔE_p was 59 mV at scanning rates up to 0.50 V s^{-1} suggesting ideal reversibility at the electrode. The open tube ends of MWNTs microbundle electrode should be responsible for the fast electron-transfer kinetics. An elegant experiment was carried out to compare the electrochemical properties of tube ends and sidewalls of CNTs by employing a bundle of superlong (~ 5 mm) VACNTs.[45] The sidewalls or tube ends were selectively masked with a nonconductive polymer to limit the electrolyte access to tube ends or sidewalls and hence, only region-specific electron transfer between the electrochemical probe molecular and CNT electrodes could be observed. It was observed that the electrochemical properties of several analytes are very sensitive to the exposed CNT region and the oxidation state of the region. For example, the electron-transfer kinetics of $Fe(CN)_6^{3-/4-}$ redox are enhanced at the tube ends, especially in the presence of oxygen-containing moieties, but slower and less pronounced at the sidewalls. In contrast, electrochemical oxidation of H_2O_2 occurs more readily on the sidewalls than tube ends, but is relatively insensitive to the presence of oxygen-containing groups. Ascorbic acid (AA) oxidation can be promoted by oxygen-containing groups but there is little difference between the tube ends and sidewalls. Since the sidewalls of the CNTs used in that study are not free of defects,[46] which can ensemble graphite edge planes to facilitate the electron-transfer kinetics. These results enable better understanding of the electrochemical behavior of CNTs. The sidewalls are not always the electrochemically inert sites and the electrochemical activity there depends on the fundamental aspects of the density of the exposed edge planes and oxygen-containing groups that dominate the electrochemical behaviour of carbon electrodes.

2.2 Carbon nanofibers

CNFs constitute a subclass of carbon nanostructured materials consisting of curved graphene layers arranged as stacked cones, cups, or plates with an angle ranging from 0 to 90° between the axis and graphene sheet.[17,26] VACNFs are produced with a high degree of control usually by catalytic PECVD (C-PECVD) procedures. The stacked cone structure is often referred to as herringbone (also termed as fishbone) as
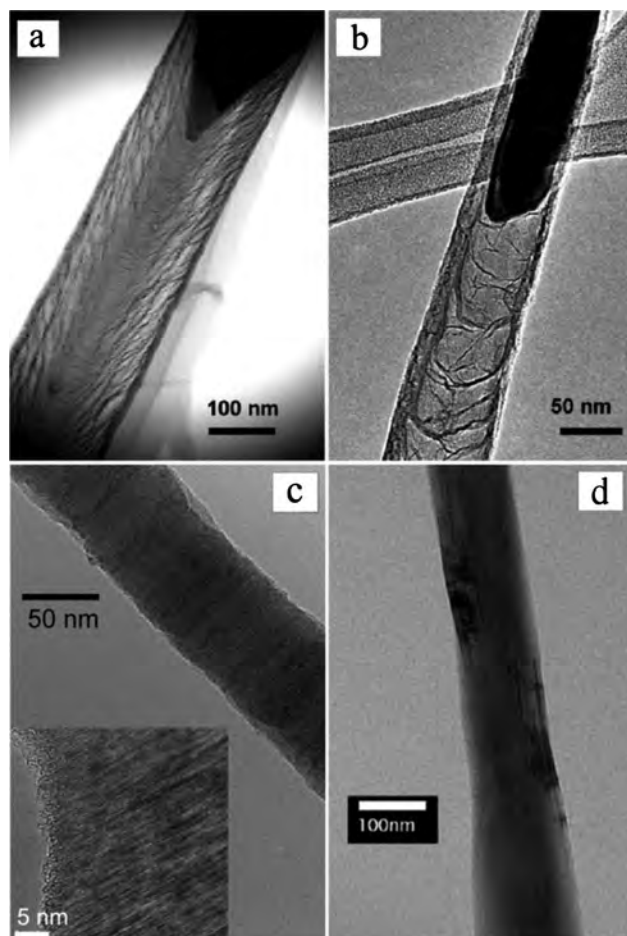
Fig. 2 (a) Scanning transmission electron microscope (STEM) image of a herringbone-like CNF produced by dc C-PECVD with Ni catalyst; (b) Transmission electron microscope (TEM) image of a bamboo-type CNF grown at the same conditions with Fe catalyst; (c) TEM images of stacked graphene nanofibers, inset: the high-resolution TEM (HRTEM) of edge of stacked graphene nanofibers; (d) TEM image of multiwalled CNTs. (a) and (b) Reprinted with permission from ref. 17, copyright 2005 American Institute of Physics. (c) and (d) Adapted from ref. 26 with permission from the PCCP Owner Societies.

their cross-sectional images resemble a fish skeleton (Fig. 2a), whereas the stacked cup structure is often referred to as a bamboo (Fig. 2b) resembling the compartmentalized structure of a bamboo stem. Recently, a new type of CNFs, platelet graphite nanofibers (PGNFs), has been fabricated by bottom-up growth.[47] These stacked graphene nanostructures consist of a large number of graphene nanosheets with a longitudinal dimension of several micrometres.[20,26]

PGNFs have a perpendicular orientation of the graphene sheets to the long axis of the fiber consequently exhibiting a large number of edge-plane sites (Fig. 2c), that are much larger than the density of such sites on the CNT surface (Fig. 2d).

The location, diameter, length, shape, chemical composition, and orientation of CNFs can be readily controlled by the CVD process.[48–51] Deliberate modulation of growth parameters results in modulation of the CNF internal structure, and this property can be used to control the CNF surface along its length to achieve site specific chemistry and electrochemistry.

The growth control mechanisms, catalyst preparation, resultant carbon nanostructures, and VACNF properties have been extensively discussed in some previous papers.[17,52] The surface properties of nanostructured materials are of special significance because they often deviate substantially from the bulk materials properties due to differences in the physical structure, chemistry, and dynamic environment. Surface analytical techniques for CNFs, for example, scanning probe microscopy, infrared and electron spectroscopies, electron microscopy, ion spectrometry, temperature-programmed desorption, and atom probe analysis have been comprehensively reviewed by Simpson and co-workers.[53]

2.3 Core-shell carbon nanofibers

PGNFs with a 90° angle between the fiber axis and stacked graphene sheets expose the edge planes almost entirety and should exhibit favorable electrochemical activity as well as superior chemical activity in biochemical immobilization.[47] However, the obtained ΔE_p value towards the $Fe(CN)_6^{3-/4-}$ redox couple at the PGNFs electrode is 174 mV which is much larger than that at the aligned CNTs or some other carbon-based nanomaterials.[24,54] This seems to contradict our previous knowledge that the higher density of exposed edge plane sites leads to higher electrochemical activity. Considering the anisotropy of crystal graphite, the in-plane resistance is 4×10^{-5} Ω cm, which is much smaller than that of inter-plane resistance of 0.17 Ω cm.[14] We may come to the deduction that the electron transfer process may be impeded along the axis of PGNFs due to the high resistivity. That is to say, large exposed edge-planes will compromise the conductivity of the C electrode and in turn degrade the electrochemical properties. However, if the core–shell CNF with a high conductive core is constructed, this dilemma to maintain both large exposure of edge-planes and high conductivity of C electrode can be circumvented because the high conductive core facilitates electron transfer. Titanium has a low contact resistance with carbon nanomaterials being about an order of magnitude smaller than that of Pd, Pt, Cu, and Au and is commonly used as a buffer layer during the fabrication of carbon nanomaterials on metallic or Si substrates.[55,56] We have recently developed several strategies to prepare core–shell structured CNF arrays on Ti or Ti alloyed substrates *via* catalyst-free methods that do not require a foreign metallic catalyst or template. The core–shell CNFs not only exhibit extremely fast electron transfer rates, but also provide versatile morphology-dependent electrochemical activity and cell-repelling properties.[57,58]

Conical core–shell nanofiber arrays consisting of TiO_2 nanowire cores and carbon shells have been produced directly on titanium foils by a simple one-step thermal reaction under acetone vapor at 850 °C.[59] The nanowire cores are single-crystalline rutile TiO_2 and the conical carbon shells have gradually decreasing thicknesses from 200–300 nm at the bases to 5–10 nm at the tips. The core–shell TiO_2/C nanofibers exhibit well-defined redox peaks towards the $Fe(CN)_6^{3-/4-}$ redox couple and sensitive determination of dopamine (DA) at a very low detection limit of 2.45×10^{-8} M.[60] Further investigation reveals that the morphology of the core–shell TiO_2/C nanofibers depends largely on the temperature of the
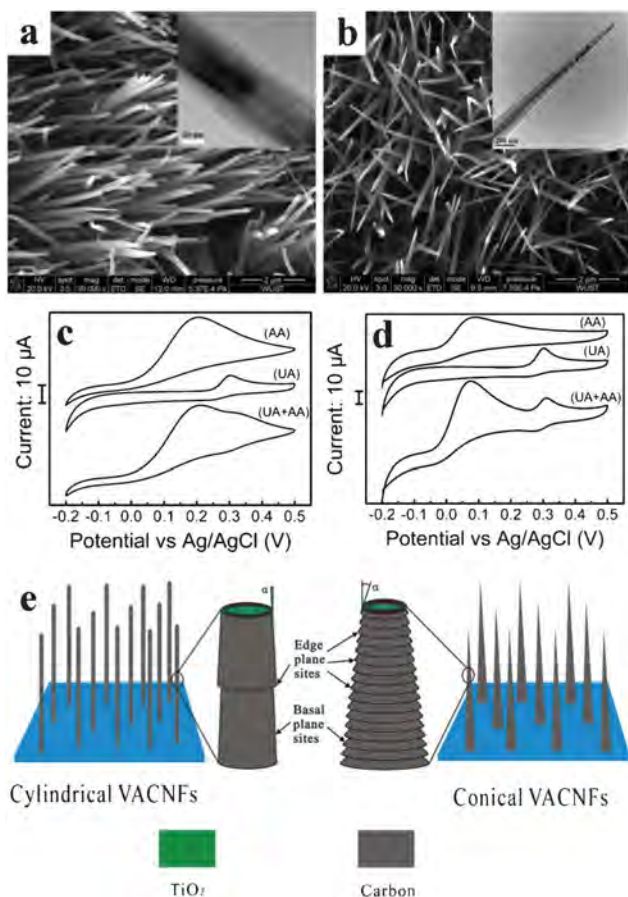
Fig. 3 (a) Scanning electron microscope (SEM) images of (a) cylindrical and (b) conical core–shell TiO_2/C nanofibers. Cyclic voltammetry (CV) graphs of 0.1 mM UA, 1.0 mM AA, and the mixer of 0.1 mM UA, 1.0 mM AA in 0.1 M phosphate buffer (pH = 7.4) at (c) cylindrical and (d) conical core–shell TiO_2/C nanofibers at a scanning rate of 5 mV s^{-1}. (e) Proposed microstructure models of cylindrical and conical core–shell TiO_2/C nanofibers. Scale bars: (a) 2 μm, 20 nm (inset); (b) 2 μm, 200 nm (inset). Reprinted with permission from ref. 27, copyright 2011 Wiley-VCH Verlag GmbH&Co. KGaA.

thermal reaction and ranges from conical to cylindrical nanofiber arrays.[27] The cylindrical nanofiber arrays have a uniform carbon shell and TiO_2 nanowire core (Fig. 3a), whereas the TiO_2/C nanocone arrays have a uniform TiO_2 nanowire core but variable carbon shell thicknesses giving rise to the conical shape (Fig. 3b). Reversible voltammetric responses to the $Fe(CN)_6^{3-/4-}$ redox couple are observed from the cylindrical and conical core–shell TiO_2/C nanofibers at scanning rates between 10 and 500 mV s^{-1}, with ΔE_p values of 69–101 mV and 63–68 mV, respectively. According to the ΔE_p values measured at a scanning rate of 500 mV s^{-1}, k^0 is 0.010 cm s^{-1} and 0.062 cm s^{-1} for $Fe(CN)_6^{3-/4-}$ on the cylindrical and conical nanofibers, respectively, indicating higher electron transfer (ET) rates on the conical nanofibers. The global coverage of the edge plane sites on the cylindrical and conical nanofibers is estimated to be 2.5% and 15.5%, respectively. The results suggest that the morphology of the CNFs is an important factor affecting the exposed edge plane sites that account for the electrochemical activity.

Voltammetric responses of uric acid (UA), ascorbic acid (AA), and their mixture on the cylindrical and conical nanofibers are shown in Fig. 3c and 3d, respectively. The results suggest that more exposed edge plane sites decrease the over-potentials and increase the voltammetric resolution. According to the Raman spectra, the D-band and G-band (I_D/I_G) ratios of the cylindrical and conical nanofibers are estimated to be 1.68 and 1.21, respectively, suggesting a larger density of edge plane sites on the cylindrical nanofibers than the conical nanofibers.[20,46] The efficacy of the electrochemical activity of a carbon electrode cannot be simply judged by the I_D/I_G ratio alone since the density of the edge plane sites determined by Raman scattering is not necessarily equal to the density of the exposed edge plane sites. The microstructure of the cylindrical and conical core–shell TiO_2/C nanofibers can be depicted as "kaleidoscope" and "Christmas tree", respectively (Fig. 3e) to distinguish the difference in the exposed edge plane sites. The cylindrical TiO_2/C nanofiber has a nanotubular shell with a large amount of defects and smaller sp^2 domains. Graphitic edge plane sites that inevitably exist at the edge are attributed to the discontinuity of graphite planes. The gradually decreasing thickness of the C shell leads to a quantum process in which the graphene layers are reduced one by one and the edges of different graphene sheets end at the sidewalls. Hence, the exposed graphitic edge plane sites on the "Christmas tree" are more abundant than those on the "kaleidoscope" and the conical CNFs possess better electrochemical activity than the cylindrical CNFs.

In view of the semi-conductive properties of TiO_2 nanowires, the electrochemical activities of core–shell CNFs can be further improved by configuring highly conductive nanowire cores instead. A one-step thermochemical process has been demonstrated to produce core–shell TiC/C nanofibers directly on biomedical Ti6Al4V alloy substrates in the absence of a foreign metal catalyst or template.[57,61] The TiC core has a uniform diameter of about 40–50 nm and the carbon shell is about 15–20 nm thick (Fig. 4a). Since the TiC/C nanofibers produced directly on the Ti alloy consist of highly conducting TiC cores and C shells possessing abundant edge-plane-like defects (Fig. 4b), the nanostructures exhibit excellent electrochemical characteristics, for example, the ideal reversibility of the $Fe(CN)_6^{3-/4-}$ redox couple on TiC/C nanofibers with a constant ΔE_p of 59 mV at scanning rates between 10 and 1000 mV s^{-1} (Fig. 4c). Selective and simultaneous determination of AA, DA, and UA in the presence of the other species is demonstrated (Fig. 4d). These biomolecules usually produce overlapping voltammetric responses on conventional bare metal or carbon electrodes. The ΔE_p value of DA measured from the TiC/C nanofibers is 29 mV corresponding to the reversible two-electron oxidation process. The excellent electrochemical behavior can be ascribed to the good electrical contact between the directly grown TiC/C nanofibers and conducting Ti alloy as well as the carbon shell and highly conducting TiC nanowire core offering an ideal transport pathway for electrons. The TiC/C nanofibers also show sensitive detection of hydrazine, with a linear range from 0.1 to 1635 μM and a low detection limit of 0.026 μM.[62] Incorporation of both high sensitivity and good selectivity electrochemical sensors into microfluidic chips is still
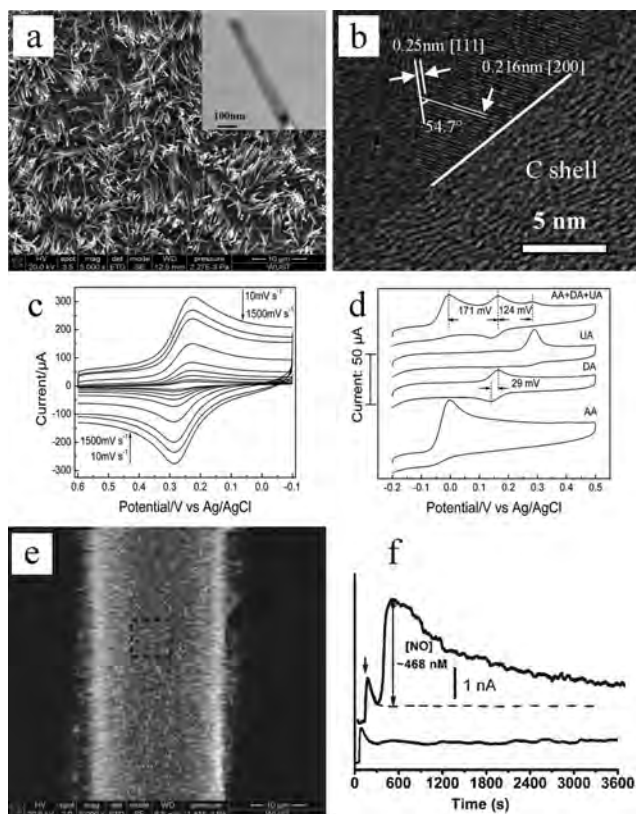
Fig. 4 (a) SEM images of core–shell TiC/C nanofibers, inset: TEM images of a TiC/C nanofibers, (b) HR-TEM images of core–shell TiC/C nanofibers, (c) CV profiles acquired from core–shell TiC/C nanofibers in 1.0 M KCl solution containing 1.0 mM $K_3Fe(CN)_6$ at scanning rates between 10 and 1000 mV s^{-1}, (d) CV graphs of 0.1 mM UA, 0.1 mM DA, 1.0 mM AA, and the mixer of 0.1 mM UA, 0.1 mM DA, 1.0 mM AA in 0.1 M phosphate buffer (pH = 7.4) at core–shell TiC/C nanofibers at a scanning rate of 100 mV s^{-1}, (e) SEM images of core–shell TiC/C nanofiber arrays microelectrode, (f) real-time amperometric detection without endothelial cells (bottom panel) and with confluence endothelial cells (upper panel) by introducing 100 mM ATP stimulating from one end of the gelatin lumen at 5 μL min^{-1}. (a), (c) and (d) Reproduced from ref. 57 with permission from The Royal Society of Chemistry. (b) Reprinted with permission from ref. 61, copyright 2012 American Chemical Society. (e)–(f) Reproduced from ref. 63 with permission from The Royal Society of Chemistry.
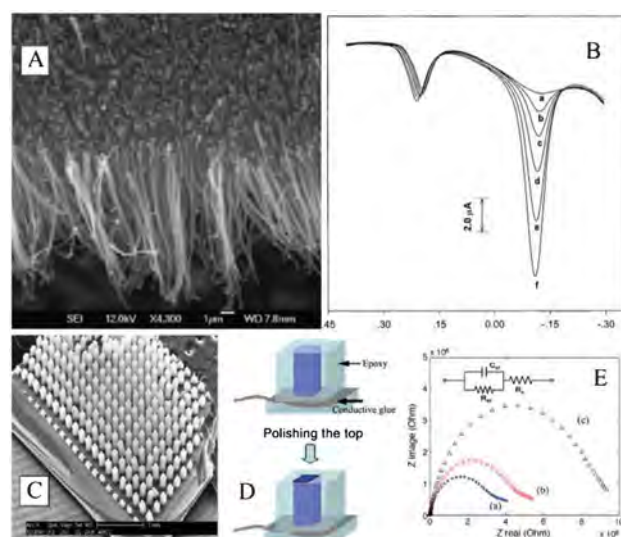

Fig. 5 (A) Scanning electron microscopy (SEM) image of the VACNTs, (B) DPV response of 5.0 μM UA at the VACNTs electrode in pH 7.4 PBS with the addition of a) 0, b) 50, c) 100, d) 200, e) 300 and f) 400 μM AA, (C) aligned CNT arrays on Si substrate, (D) procedure for mechanical polishing of CNTs tips, and (E) Electrochemical impedance spectra for a nanotube electrode, after: (a) activated nanotube array; (b) immobilized with Donkey anti-mouse antibody IgG; and (c) binding to mouse IgG; at 0 V over a frequency range between 0.1 Hz and 300 kHz. The sinusoidal potential magnitude is ± 20 mV in 5.0 mM $K_4[Fe(CN)_6]$ and 0.5 mM $K_3[Fe(CN)_6]$ in PBS (pH 7.0). (A) and (B) Reprinted with permission from ref. 64, copyright 2003 WILEY-VCH Verlag GmbH&Co. KGaA. (C), (D) and (E) Reprinted with permission from ref. 73, copyright 2007 Elsevier B.V.

challenging. By introducing core–shell TiC/C nanofiber arrays *in situ* grown on a Ti6Al4V microwire (Fig. 4e) to a three-dimensional gelatin chip, highly sensitive and real-time monitoring of NO generation from the vascular-like lumen is demonstrated, with detection limits down to sub-nM (Fig. 4f).[63] The TiC/C nanofibers display super-hydrophobicity with a water contact angle of 137.5° that can minimize surface fouling in aqueous solution.[58] The TiC/C nanofibers also have been demonstrated to be satisfactory cell-repelling structures with good biocompatibility and long-term stability.[58]

The mechanism of this catalyst-free growth process to form core–shell TiO_2/C and TiC/C nanofibers has been proposed.[61]

Briefly, at the thermal reaction temperature of around 800 °C, acetone is decomposed into ·CH$_3$ radicals and CO, and the CO generated *in situ* preferentially reacts with Ti to form TiO_2. At the same time, carbon atoms are produced by decomposition of ·CH$_3$ radicals on the surface of TiO_2 to form the carbon

shell. As the reaction proceeds, more Ti atoms diffuse outward from the bulk through the boundary of the formed TiO_2 and react continuously with CO to form more TiO_2. Finally, core–shell TiO_2/C nanofibers are produced on the Ti foil. When Al is introduced into the surface, Ti preferentially reacts with C forming TiC rather than reacting with CO to produce TiO_2 because the Gibbs free energy of the reaction between Al and CO to produce Al_2O_3 is more negative than that between Ti and CO to form TiO_2. Moreover, Al can reduce TiO_2 to Ti because of the negative Gibbs free energy of the reaction. Consequently, in the presence of Al, core–shell TiC/C instead of TiO_2/C nanofibers are produced.

3. Microelectrode arrangements

3.1 Vertically aligned microelectrode arrays

VACNTs produced by CVD offer many advantages over randomly distributed CNTs for constructing electrochemical sensors, such as directly electrical connection to the substrates, highly exposed tube ends that facilitate heterogeneous electron transfer rates, and precisely controllable morphology and quality. VACNTs grown on a thin layer of cobalt by CVD strategies without plasma aid have diameters of 80 to 120 nm and a length of about 10 μm (Fig. 5A).[64] Compared to glassy carbon (GC) electrode, VACNTs electrode catalyzes electrochemical oxidation of UA and AA by reducing the overpotentials of 0.028 V and 0.416 V, respectively. Meanwhile, the

VACNTs electrode resolves the overlapping voltammetric response of UA and AA into two well-defined voltammetric peaks in applying both CV and differential pulse voltammetry (DPV) (Fig. 5B). And selective determination of UA in the presence of AA in human urine samples by the VACNTs electrode has been successfully carried out with high sensitivity and reliability. Indirect determination of acetylsalicylic acid has been demonstrated by a VACNTs electrode.[54] VACNTs were synthesized on Ta-plate by CVD using ethylenediamine as the carbon source and cobalt as the catalyst. The VACNTs have diameters ranging from 80 to 120 nm and a length of about 10 μm. The VACNTs electrode shows very fast electron transfer kinetics towards $Fe(CN)_6^{3-/4-}$ redox couple with a ΔE_p value of around 60 mV at scan rate up to 1 V s^{-1}, suggesting an ideal Nernst behavior at the electrode. Compared to GC electrode, the VACNTs electrode displays enhanced sensitivity as well as larger response linear range for acetylsalicylic acid determination.

The electrochemical activity of CNTs can be improved by depositing noble metal nanoparticles on the tips.[65] VACNTs synthesized by CVD have diameters of 20 nm and lengths of approximately 8 mm. After treatment with oxygen plasma, gold nanoparticles are electrochemically deposited on the VACNTs tips at a constant potential of 1.0 V. By using a 6.0 mM $K_3Fe(CN)_6$ solution as the electrochemical probe, the CV peak currents increase with electrodeposition time and ΔE_p values decrease with electrodeposition time, indicating enhanced electron transfer kinetics by deposition of gold nanoparticles. Moreover, the deposited gold nanoparticles can be used for biomolecules immobilization and biosensor development. A highly sensitive electrochemical sensor to determine L-cysteine based on Pt nanoparticles modified VACNTs has been proposed.[66] The electrode exhibits a higher electrocatalytic activity towards oxidation of L-cysteine than GC electrode. The linear range between 1 and 500 μM and an outstanding sensitivity of 1.42×10^3 μA mM^{-1} cm^{-2} is achieved at an applied potential of +0.45 V. The Pt nanoparticles modified VACNTs electrode has been applied to the determination of L-cysteine in human urine samples with satisfactory analytical performance, thus demonstrating its potential in practical applications.

CNTs catalytically produced on metal substrates often suffer from high capacitive currents, limited reproducibility, or complicated data interpretation inherent to spatial heterogeneity.[67] In some cases, the metal catalyst residue trapped in the CNTs can even dominate the electrochemical response.[68,69] As revealed by Pumera et al., even 0.01 wt% of metal impurities can significantly influence the electrochemistry of CNTs.[70] To overcome these difficulties, a VACNTs electrode was fabricated by passivating the original substrate and removing the metal catalyst nanoparticles on the tip of the CNTs.[71] A thin layer of silicon oxide 20 nm thick was sputtered on the substrate, followed by sputtering of a 4 nm thick Fe film. After fabricating the VACNTs by PECVD, the electrode was immersed in 2 M nitric acid to remove the metal catalyst nanoparticles and the amorphous carbon sheath covering the nanotubes is removed by water plasma which etched the amorphous carbon by oxidation. The resulting nanotubes were densely packed with open tube ends. The as-prepared VACNTs

electrode displayed a highly reversible electrochemical behavior, with ΔE_p around 70 mV at a scanning rate up to 2 V s^{-1} in the CV measurement. The low capacitive currents were also beneficial to the use of the electrodes in electroanalysis. The plasma treated tube ends had abundant hydroxyl and carboxyl terminations rendering them suitable for immobilization of enzymes or antibodies for biosensing.

Mechanical polishing of CNTs tips can also remove the metal catalyst nanoparticles and open the tubes ends of CNTs. VACNTs have been synthesized by CVD in a horizontal tube furnace, using ethylene as the carbon source and iron film as the catalyst.[72] The VACNTs that have an average diameter of 20 nm and length of 4 mm are aligned in a high density of approximately 25 million nanotubes per mm^2, as shown in Fig. 5C. After the substrate is peeled off, the VACNTs are encapsulated by epoxy (Fig. 5D). Both ends of the VACNTs electrode are polished with one end for electrical connection and the other exposed as the working electrode. The polished VACNTs are uniform in length and diameter. Compared to other carbon materials such as GC, carbon black, carbon fibers, and pyrolytic graphite, the edge-planes are readily accessible due to the geometry of the open-ended nanotube array. Well-defined voltammograms are obtained at scanning rates up to 5 V s^{-1} for both the $Fe(CN)_6^{3-/4-}$ redox couple and $Ru(NH_3)_6^{3+/2+}$ redox couple. The polished VACNTs electrode can be electrochemically activated to expose the COOH groups on the surface for anti-mouse IgG immobilization.[73] Immobilization of the antibody has been carried out by N-(3-dimethylaminopropyl)-N'-ethylcarbodiimide (EDC) and N-hydroxysuccinimide (NHS) procedures. Electrochemical impedance spectroscopy (EIS) is performed to determine the mouse IgG (Fig. 5E). A detection limit of 200 ng mL^{-1} and dynamic range up to a 100 μg mL^{-1} are achieved. Reliable and reproducible fabrication of CNTs electrode by mechanical polishing of VACNTs has been reported.[74] The electrode has low background currents and desirable voltammetric behavior towards NADH. Moreover, mechanically polished VACNTs are found to be robust and can be reproducibly renewed many times by mechanical polishing followed by O$_2$ plasma treatment.

VACNFs can be synthesized with a wide range of sizes from nanoscale, individual elements to large, wafer-scale, to forests. Many microfabrication processes have been employed to synthesize CNFs, for example, refractory metal reactive ion etch, oxide coating and removal, and several oxygen-based etching processes.[75] On the microscale, the processing effects can have a dramatic impact on nanofiber electrochemistry. With regard to the diffusion-limited macroscale electrode, the surface area enhancement rendered by the high-aspect ratio morphology of the VACNFs may serve as a buffer to the same processing effects. The buffering capacity also may help to preserve the performance of the nanofiber electrodes temporally, thereby minimizing the need for activation procedures as required for many conventional forms of carbon electrodes.

By decomposition of hydrocarbon or carbon monoxide over a surface of metal catalyst, diverse one-dimensional carbon nanomaterials have been successfully synthesized. However, the catalytic CVD method requires complicated steps including preparation and removal of the metal catalysts.[76,77] The

encapsulation of the metal catalyst is difficult to take away completely even after treatment in strong acids for a long time.[68] The metal impurities not only lead to potential misinterpretation of electrochemical signals, but also significantly affect the electrochemical reproducibility and stability.[70,78] Using anodic aluminum oxide (AAO) nanotube arrays as the template and petroleum pitch as the precursor, a catalyst-free method has been developed for massive production of uniform CNF arrays.[79] The diameter and length were 300 nm and 60 μm, respectively. The difference between these CNFs and the classic herringbone-like structure is that the angle between the graphene and fiber axis increases regularly along the axis instead of being fixed. The nanofiber consists of stacked conical graphenes with cone angles that steadily increase from 60° to 180° (amounting to 30° to 90° of the angle in Fig. 1d) along the fiber axis. The spacing between the graphitic planes gradually becomes narrower from periphery to center. The morphology and microstructure of the CNFs can be controlled based on the surface affinity between the template and precursor. However, there is still a challenge for the AAO template method, especially in finding a facile procedure to fabricate well-aligned and free-standing CNF arrays on a substrate after dissolution of the AAO membrane. Using the nonionic triblock copolymer as a soft template and AAO membranes as hard templates, well-aligned freestanding CNF arrays have been fabricated on silicon wafers.[80] The hexagonal-arranged circular mesochannels located at the edge of the CNFs and columnar oriented mesochannels and wrapped by the circular mesochannels form at the center of certain nanofibers. The surface interaction with the alumina pore walls is probably responsible for the formation of both circular and columnar oriented mesochannels. Recently, it is proposed that catalyst-free strategies do not require a metal catalyst or template to prepare core–shell structured CNF arrays on Ti or Ti alloy substrates.[27,57,59] The core–shell CNFs which consist of a TiO_2 or TiC nanowire core and carbon shell exhibit very interesting electrochemical behavior that depends on the morphology of the nanofibers as well as composition of the nanowire cores, as discussed above in detail.

3.2 Self-assembly microelectrode arrays

The tube ends of the CNTs not only exhibit high electrochemical activity, but also can be readily bonded to biological molecules to accomplish selective and sensitive biosensing. Moreover, owing to the small size, CNTs are attractive materials in probing electron transfer reactions between the redox centers of the proteins and tube ends of the CNTs.[81,82] The electrode is modified with CNTs by dip coating a random tangle of nanotubes onto the electrode surface resulting in an unknown spatial relationship between the redox proteins and nanotubes. The chemically shortened CNTs can be aligned to the surface of a gold disk electrode by self-assembly and act as molecular wires to allow electrical communication between the underlying electrode and redox proteins covalently attached to the ends of the CNTs.[42] Fig. 6a illustrates the detailed procedures of self-assembly CNTs on a gold electrode.[83] An amino and thiol contained bifunctional compound is employed to form a monolayer-coated gold surface simply by immersing the gold electrode in the bifunctional compound
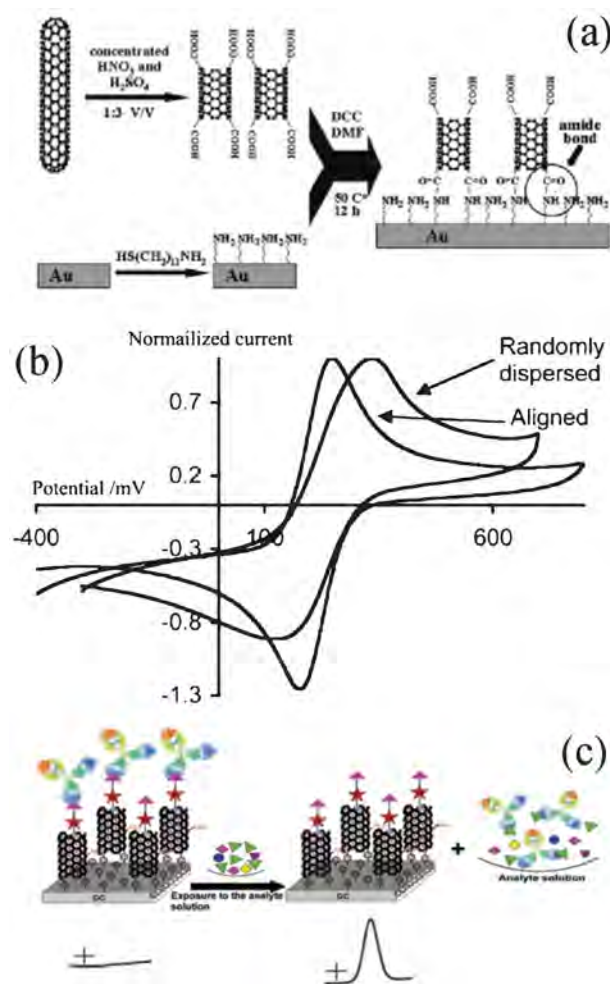

Fig. 6 (a) Schematic representation of the formation of SWNT assemblies, (b) CV graphs of 1 mM K3Fe(CN)6 at CNTs modified electrodes where the tubes were cut for 2 h and either randomly dispersed or vertically aligned, (c) Scheme of an electrochemical immunosensor based on self-assembly CNTs for direct detection of the pesticide endosulfan. (a) Reprinted with permission from ref. 83, copyright 2005 American Chemical Society. (b) Reproduced from ref. 84 with permission from The Royal Society of Chemistry. (c) Reprinted with permission from ref. 88, copyright 2012 American Chemical Society.

solution. The CNTs are shortened by treatment in a strong acid leaving the –COOH groups on the tube ends. The $-NH_2$ groups on the top of the monolayer-coated gold surface chemically condense with the –COOH groups at the end of CNTs by using dicyclohexylcarbodiimide (DCC) as the condensing agent. CV graphs indicate that the assembled CNTs allow electron communication between the gold electrode and redox couple in the solution. The distance between the assembled CNTs is on the order of tens of nanometers, whereas the diffusion layer thickness in typical experimental timescales is tens micrometers. Therefore, the diffusion layers of the individual CNTs overlap substantially and produce electrochemical behavior similar to that of macroelectrodes. Self-assembled CNTs exhibit faster heterogeneous electron transfer than randomly distributed CNTs, as shown in Fig. 6b.[84] The reason lies in the fundamental electrochemistry of CNTs. The assembled CNTs

provide a larger density of edge planes than randomly dispersed CNTs. The electron transfer rate is larger at the tube ends of CNTs but smaller at the walls. The assembled CNTs promote direct electron transfer rate between an electrode and the redox active center of glucose oxidase and flavin adenine dinucleotide.[85]

Besides the nanotube orientation, the influence of the nanotube length on the electrochemical behavior of CNTs modified electrodes has been investigated.[86] Gold electrodes are modified with either randomly dispersed or self-assembly CNTs to which ferrocenemethylamine is attached. The electron transfer kinetics is found to depend strongly on the orientation of the nanotube, with the electron transfer rate between the gold electrode and the ferrocene moiety being 40 times slower through randomly dispersed CNTs than through self-assembled CNTs. The conducting properties of SWNTs imply a resistive element in the circuit that should be proportional to the length. For the self-assembled CNTs, the rate constant of electron transfer varies inversely with the mean length of the nanotubes. The assembled CNTs on the gold surface can be further bonded to redox active molecules such as octa(hydroxyethylthio)phthalocyaninatoiron(II).[87] The electrode exhibits a strong dependence on the reaction of the head groups and pH of the working electrolytes. The high electron transfer capability of the electrode suggests that the assembled CNTs greatly improve electronic communication between the redox active molecules and bare gold electrode.

CNTs can also be covalently assembled on carbon related materials. A mixed layer of 4-aminophenyl and phenyl is covalently immobilized on GC substrate *via in situ* electro-grafting of the aryldiazonium salts in acidic solutions.[88] The CNTs are then covalently and vertically anchored on the electrode surface *via* the formation of amide bonds from the reaction between the amines located on the modified GC surface and the carboxylic groups at the tube ends of CNTs. On account of the aryldiazonium salt chemistry, the stability of the assembled CNTs has advantages over self-assembly strategies of alkanethiols on gold.[89] Ferrocenedimethylamine is subsequently attached to the ends of CNTs by amide bonding followed by attachment of endosulfan hapten to which antiendosulfan IgG binds. Association or dissociation of the antibody modulates the ferrocene electrochemistry, as shown in Fig. 6c. The fabricated electrochemical immunosensor can be applied to determine endosulfan over the range of 0.01–20 ppb at a detection limit of 0.01 ppb.

3.3 Low density microelectrode arrays

As aforementioned, the diffusion profile of the MEAs depends on the electrode size and space between each individual microelectrode. With regard to an individual microelectrode, the characteristic time, t_c, of a CV experiment has significant influence on the diffusion profile.[4] The characteristic time can be expressed by the reciprocal of the scanning rate: $t_c = \dfrac{RT}{NFv}$. When $r_0 \gg \sqrt{Dt_c}$, where r_0 is the radius of a microdisk electrode, the voltammogram will appear as predicted for a macroelectrode. On the other hand, when $r_0 \ll \sqrt{Dt_c}$, the voltammogram will take on a sigmoidal shape for a Nernstian reduction and between the two limits, the shape of the voltammogram depends on the ratio
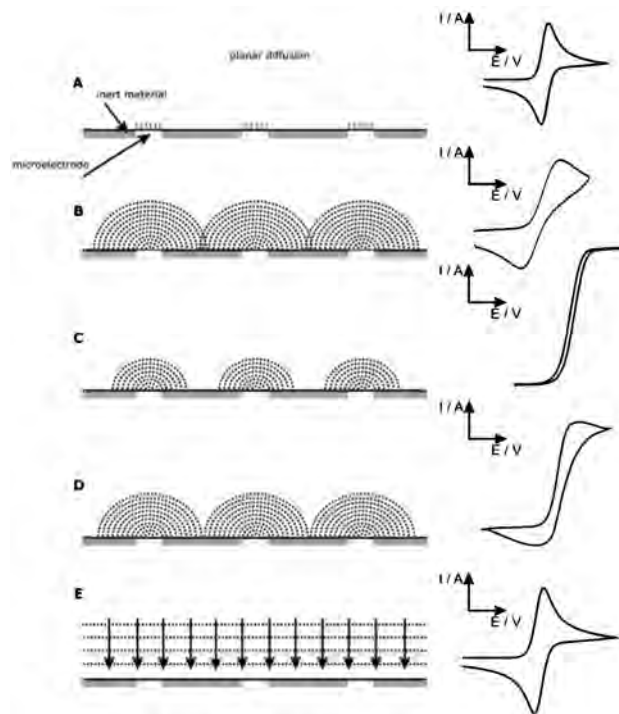

Fig. 7 Schematic diagram of the categories a diffusion profile may take at a microelectrode array. Reproduced from ref. 90 with permission from The Royal Society of Chemistry.

of $\dfrac{r_0}{\sqrt{Dt_c}}$. The diffusion zones greatly influence the electrochemistry of MEAs and produce voltammetric profiles ranging from sigmiodal shape to peak shape. There are five main categories for MEAs,[90] as shown in Fig. 7. In brief, the diffusion layers in category A are small compared to the magnitude of the microdisks comprising the array resulting in planar (linear) diffusion. The voltammetric profile has a peak shaped and the response of the microelectrode array is that of an isolated macro-electrode multiplied by the total number of disks comprising the array. In category B, the diffusion zones overlap that of their nearest neighbor. The voltammetric profile is observed between planar and hemi-spherical, depending on the scanning rate of the CV graphs. In category C, the diffusion layer is large in magnitude relative to the microdisks but adjacent diffusion layers do not interact. The observed voltammetric profile has steady-state characteristics which are usually observed from a single microdisc multiplied in magnitude by the total number of microelectrodes in the array. In category D, a mixed diffusion regime is encountered between planar and hemi-spherical diffusion. In category E, the diffusion zones exceed the insulating space between microdisks resulting in complete overlap between the diffusion zones and planar diffusion regime.

The voltammogram of closely packed CNT arrays is similar to that of a macroelectrode such as graphite or glassy carbon since the diffusion layer overlaps substantially. To achieve a sigmiodally shaped voltammetric profile as shown in Fig. 7C, the inter-spacing of the individual CNT should be much larger than the radius of the CNT. Therefore, low-density CNT arrays have been developed by controlled distribution of the metal
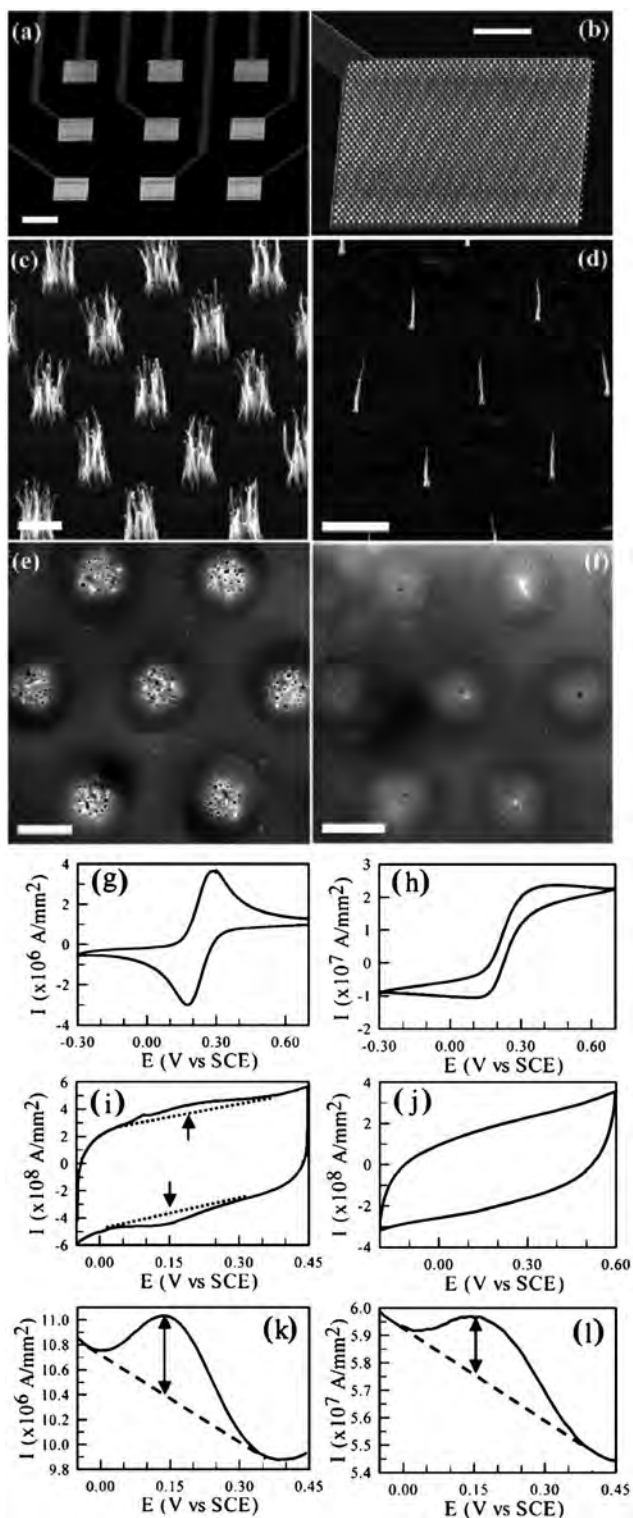
catalyst on the substrate. Combining micro- and nanolithography with CVD, a bottom-up approach has been developed to fabricate low-density CNT arrays.[91] A 3 × 3 array of individually addressable Cr film is patterned on a Si(100) wafer by UV-lithography, as shown in Fig. 8a–b. After depositing a 10 to 20 nm thick Ni catalyst film on the Cr film, catalytic growth of VACNTs by PECVD is carried out on 2 μm and 200 nm diameter Ni spots defined by UV and e-beam lithography, respectively (Fig. 8c–d). The diameter of CNTs, number of CNTs at each spot, as well as spacing and spot size can be precisely controlled. Single nanotubes can be grown at each catalyst spot if the size is reduced to below 100 nm. The as-grown CNTs are encapsulated with a SiO$_2$ film by tetraethoxysilane CVD, followed by mechanical polishing to expose the tube ends (Fig. 8e–f). The CV curve of the high-density array (Fig. 8g) is similar to a macroelectrode due to the large overlap of the diffusion layer from each CNT electrode. The CV feature dramatically changes to a sigmoidal steady-state curve for the low-density sample (Fig. 8h), indicating that CNTs approach independent nanoelectrodes as they are separated sufficiently. Fig. 8i–j show the CV curves of the two CNT array electrodes after functionalization with the ferrocene (Fc) derivative, respectively. For the high-density sample, a pair of waves can be seen centered around 0.16 V (indicated by the arrows), while it is almost a flat background for the low-density sample. Fig. 8k–l display very similar ACV curves in 1.0 M KCl obtained with the two CNT array electrodes functionalized with Fc, respectively. The backgrounds are stable and can be fitted with linear curves as indicated by the dashed lines. The extracted peak height is proportional to the number of Fc(CH$_2$)$_2$NH$_2$ molecules on the electrode surface.

Low-density CNT arrays not only display independent nanoelectrode behavior showing diffusion-limited steady-state currents over a wide range of CV scan rates, but also exhibit much improved sensitivity towards determination of biomolecules, such as purines and DNA/RNA.[91,92] The open-end of the low-density CNT arrays has excellent electrochemical activity similar to that of the HOPG edge planes. The unique surface chemistry facilitates selective functionalization of the tube ends with biomolecules through amide bonding. Exposure of the tube ends of low-density CNT arrays can also be achieved by polishing or O$_2$ plasma treatment to remove the embedded epoxy.[32] By coupling thermal CVD and standard lithography, low-density bundles of VACNTs can be produced directly on a planar carbon film with controlled electrode spacings and diameters (down to 2 μm). The voltammograms show well-defined, steady-state responses consistent with each electrode functioning independently and negligible overlap of neighboring diffusion fields. The procedures are suitable for mass production of electrode arrays and integration of arrays into larger devices. The low-density bundles of CNTs are expected to combine the electroanalytical advantages of

Fig. 8 SEM images of (a) 3 × 3 electrode array, (b) array of CNT bundles on one of the electrode pads, (c) and (d) array of CNTs at UV-lithography and e-beam patterned Ni spots, respectively, (e) and (f) the surface of polished CNT array electrodes grown on 2 μm and 200 nm spots, respectively. Panels (a–d) are 45° perspective views and panels (e–f) are top views. The scale bars are 200, 50, 2, 5, 2, and 2 μm, respectively. (g) and (h) CV measurements in 1 mM K$_4$Fe(CN)$_6$ and 1.0 M KCl; (i) and (j) CV measurements of Fc derivative functionalized CNT array electrodes in 1.0 M KCl solution; and (k) and (l) AC voltammetry measurements at 50 Hz and an amplitude of 50 mV on the staircase DC ramp from 0.55 to 1.20

microelectrodes with the attractive properties of VACNTs, which typically give fast rates of electron transfer for redox probes and a high concentration of surface carboxylate groups for facile electrode modification.

The metal catalyst distribution can be precisely controlled by standard micro- and nanolithography for growth of low-density CNTs. However, lithography is always laborious, slow, and costly for electrode fabrication. Consequently, alternative techniques are employed for metal catalyst distribution. Electrochemical deposition has been used to prepare Ni nanoparticles as the catalysts for the growth of aligned CNTs. The nucleation site density of the Ni nanoparticles is controlled by the magnitude and duration of the pulse current.[93] The site density of the aligned CNTs grown by PECVD from the nickel nanoparticles varies from 10^5 to 10^8 cm^{-2}. The as-grown CNTs are then half embedded into the polymer resin, followed by mechanical polishing using a fiber-free cloth to expose the tip of the CNTs.[94] The low-density CNT arrays have quasi-reversible electrochemical reactions towards the $Fe(CN)_6^{4-}/Fe(CN)_6^{3-}$ redox couple and a sigmoidal voltammogram is expected from the microelectrode. Glucose oxidase is covalently immobilized on the low-density CNT arrays *via* carbodiimide chemistry by forming amide linkages between the amine residues and carboxylic acid groups on the CNT tips.[95] Catalytic reduction of hydrogen peroxide liberated from the enzymatic reaction between glucose oxidase and glucose and oxygen on the CNTs enables selective detection of glucose. The reaction occurring at the biosensor is very fast and reaches a dynamic equilibrium upon addition of the sample solution. A steady-state current signal is generated within 20 to 30 s. The linear response of the glucose is up to 30 mM and the detection limit is 0.08 mM based on S/N = 3. The biosensor effectively performs a selective electrochemical analysis of glucose in the presence of common interfering species. Spin-coating of an epoxy resin provides an effective passivation layer of low-density CNT arrays, resulting in reduced electrode capacitance and current leakage.[96] Sigmoidal CV curves with low capacitive current and scan-rate-independent limiting current are observed. The low-density CNT arrays have been used for voltammetric detection of trace concentrations of lead(II) ions at the ppb level. After coating with a bismuth film, the low-density CNT arrays display high selectivity for simultaneous voltammetric detection of trace cadmium(II) and lead(II) ions at the sub-ppb level and detection limit down to 0.04 ppb.[10]

3.4 Individually addressable microelectrode arrays

Microelectrodes have been demonstrated to be promising in the monitoring of chemical dynamics at the single cell level thus enabling observation of fast time-constant events in and around living cells such as the exocytotic release of neurotransmitters [5]. However, a microelectrode provides a single data point in time so that information concerning spatial heterogeneity of exocytotic events is difficult to obtain. Such information enables a better understanding of the molecular mechanisms and chemical basis for the regulation of neural secretion. By combining photolithography and PECVD, high aspect ratio VACNF arrays have been fabricated in a wafer-scale process that culminates in the realization of electro-

chemical monitoring.[33,97] Electron beam lithography is used to define the catalytic growth sites of the VACNFs. Following catalyst deposition, the VACNF is produced by PECVD. These probes are passivated with a thin layer of SiO_2 which is then removed from the tips of the VACNF by plasma etching to render them electrochemically active. The VACNFs are conical in shape and on the average has a base diameter of 200 nm, height of 1 μm, and tip radius of curvature of 20 nm. Because of the size and site-specific directed synthesis of the VACNFs, these probes are well suited for the characterization of electrochemical phenomena with an unprecedented degree of spatial resolution. The VACNF arrays can be further functionalized *via* electrochemical reactions.[98] Nitro groups on the specific nanostructures are reduced to amino groups and then used to covalently link DNA to only these nanostructures. Four-element arrays of distinct DNA oligonucleotides on CNT electrodes and the addressable functionalization of submicron bundles of VACNFs have been demonstrated. DNA hybridization shows that the DNA-modified nanoscale structures have excellent biological selectivity. Electrical control of the functionalization of high-density arrays has the additional possibility of making biochips that can be easily configured during manufacturing under simple software control. The as-grown VACNFs can be partially embedded in a UV-crosslinked epoxy membrane and peeled from their original growth substrate.[34] The membrane of VACNFs is then aligned and mated with an array of individually addressable contact pads. The transferred VACNFs are shown to retain their high-aspect-ratio morphology and the viability as electrodes, as demonstrated by electrochemical analysis and gold electrodeposition. The transfer process opens opportunities for the fabrication of a variety of devices including biomedical applications such as retinal prostheses and peripheral-nerve interfacing.

Individually addressable VACNFs can be employed as substrates for relatively long-term culture and differentiation of neuronal cells including neuronal-like derived cell lines (rat pheochromocytoma, PC-12) and primary cells (dissociated cells from embryonic rat hippocampus).[8] Electroanalysis using discrete electrodes following long-term cell culture demonstrates that this platform is responsive to the detection of easily oxidized species generated by the cultured cells. The quantal release of easily oxidized transmitters can be observed at the nanofiber electrodes following direct culture and differentiation on the arrays for at least 16 days. Stimulation and extracellular recording of the spontaneous and evoked neuroelectrical activity in organotypic hippocampal slice cultures by VACNF arrays have been demonstrated.[99] Ni catalyst dots of 100 nm thick, 2 μm in diameter, and 15 μm in spacing are defined lithographically, followed by growth of VACNFs by PECVD. After passivation and etching, the VACNF arrays consisted of a linear array of 40 individually addressable electrodes, 10 μm in height, and spaced 15 μm apart along a total length of 600 μm are examined under light (Fig. 9A) or SEM (Fig. 9B). The steady-state current of 1 mM ruthenium hexamine trichloride in 300 mM KCl is observed from the CV sweeps. The individual VACNF electrodes are conical (Fig. 9C) allowing the electrodes to penetrate into the tissue to improve electrical coupling. To record the electrical activity, a hippo-
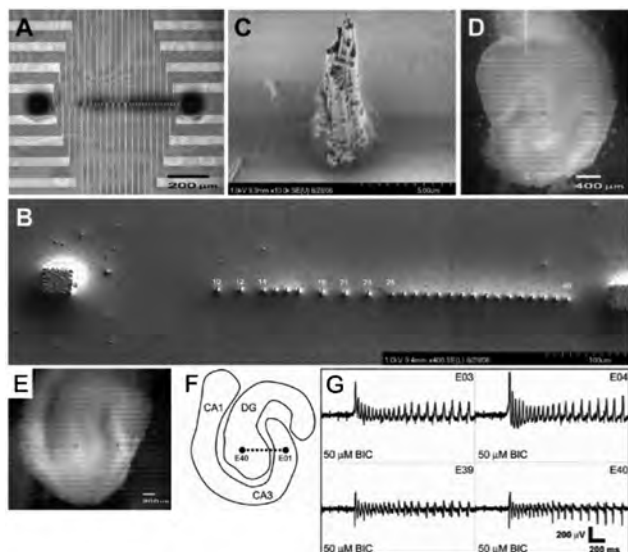
Fig. 9 Images of VACNF arrays: (A) Light micrograph of a VACNF array before use. (B) SEM image of the entire VACNF array from (A) acquired after several electrophysiological recordings. (C) An SEM image of a VACNF electrode from the same array in (B). (D) Light micrograph of a hippocampal slice (22 DIV) on the VACNF array chip. (E) A light micrograph of a hippocampal slice (13 DIV) on a VACNF array chip. (F) A schematic of the hippocampal anatomy depicts the electrode recording locations. The electrode array crossed the hilus region from the dentate gyrus granule cell layer to the CA3 pyramidal layer. (G) BIC-induced epileptiform activity as shown for four channels (electrodes 3, 4, 39, and 40). Reprinted with permission from ref. 99, copyright 2007 American Chemical Society.

campal slice is positioned on the VACNF array and oriented with respect to the anatomy (Fig. 9D). After the electrical activity is recorded, the tissue is gently removed before another culture is positioned on the VACNF array. Inhibitory neuronal circuits within the hippocampus restrict spontaneous activity under normal conditions with the majority of inhibition mediated by the GABAA receptor, which can be blocked by (−)-bicuculline methiodide (BIC). Administration of 50 μM BIC induces spontaneous epileptiform activity which is recorded with the VACNF arrays. A hippocampal slice is placed on an array crossing the hilus region (Fig. 9E) with electrode 1 in the dentate gyrus granule cell layer and electrode 40 in the CA3 pyramidal cell layer (Fig. 9F). The BIC-induced epileptiform activity propagates throughout the hippocampal slice and is detected on multiple channels (Fig. 9G). The individually addressable VACNF arrays offer many advantages such as improved biocompatibility, excellent electrochemical properties and inertness, reduced tissue response, readiness for functionalization with specific proteins, and direct neurochemical sensing through amperometry or cyclic voltammetry. They are well suited for electrophysiology and neuroscience by enabling multimode recordings (electrical and neurotransmitter) at high spatial resolution.

Multiplexed biosensors consisting of nine individually addressable VACNF arrays are fabricated by nanopatterning of Ni catalyst dots with electron beam lithography and PECVD growth of VACNFs on the nickel dots.[100] To ensure the nanoelectrode behavior with high sensitivity, VACNFs are precisely grown on 100 nm Ni dots with 1 μm spacing on each micro pad. Electrochemical detection of the hybridization of DNA targets from *E. coli* O157:H7 onto oligonucleotide probes is demonstrated. The 9 arrays within the chip are divided into three groups with triplicate sensors for the positive control, negative control, and specific hybridization. The proposed method has the potential to be scaled up to $N \times N$ arrays with N up to 10. It is ideal for detecting a myriad of organisms and can be further used as a generic platform in many electro-analysis applications. The impact of the electrode size and spacing between VACNF on the electrochemical behavior has been investigated.[35] Three types of electrodes, including standard microdisks, randomly grown VACNFs where spacing between electrodes is not fixed, and electron beam patterned VACNFs where electrode spacing is fixed at 1 μm, are employed. As the size of the microdisk electrode is reduced, the EIS spectra change from a straight line to a semicircle accompanied by huge noise which limits the sensitivity. In the case of VACNFs, the electrode spacing controls the spectra, that is, a straight line for randomly grown VACNFs and semicircle for patterned VACNFs. In contrast to microdisks, patterned VACNFs show almost insignificant noise even at small perturbations (10 mV) and linearity as the amplitude of the sinusoidal signal increases from 10 to 100 mV.

Without photolithography, individually addressable MEAs can be fabricated by assembling carbon fibers encased separately in pulled glass-capillary sheaths.[101] The carbon MEAs are composed of individually addressable 2.5 μm radius microdisks embedded in glass. The fabrication involves pulling a multibarrel glass capillary containing a single carbon fiber in each barrel into a sharp tip, followed by beveling the electrode tip to form an array of carbon microdisks. Fig. 10a shows the steady-state voltammetric response of a seven carbon fibers MEA with each electrode measured simultaneously. Fig. 10b shows an optical micrograph of a carbon MEA placed on a single PC12 cell. A glass micropipette containing a K$^+$ solution (100 mM) is positioned about 100 μm away to stimulate secretion. Fig. 10c displays a 16-min amperometric recording of exocytotic events at a single PC12 cell. Each current transient corresponds to the electrochemical oxidation of dopamine (DA) molecules secreted from a single intracellular vesicle. Amperometric results indicate that sub-cellular heterogeneity in single-cell exocytosis can be electrochemically detected with the MEAs. For example, the area of the cell membrane under electrode F (E$_F$, the same below) shows fewer events than the others during the first 8 min and appears to be a "cold spot". More interestingly, spots may be "hot" during a specific period, but then change to "cold" (or *vice versa*) after another stimulus. Close inspection of the response from E$_A$ shows that there are fewer events detected after the second and fifth stimuli than after the third and fourth ones. In addition, E$_F$ and E$_G$ clearly detect more events in the last 8 min than in the first. Hence, it appears that the array electrode format allows detection of localized membrane functions in terms of exocytosis for a single cell. Numerical simulation of the molecular flux reveals that the diffusion of DA molecules and electrochemical reactions play important roles in the temporal resolution of electrochemical imaging.[102]
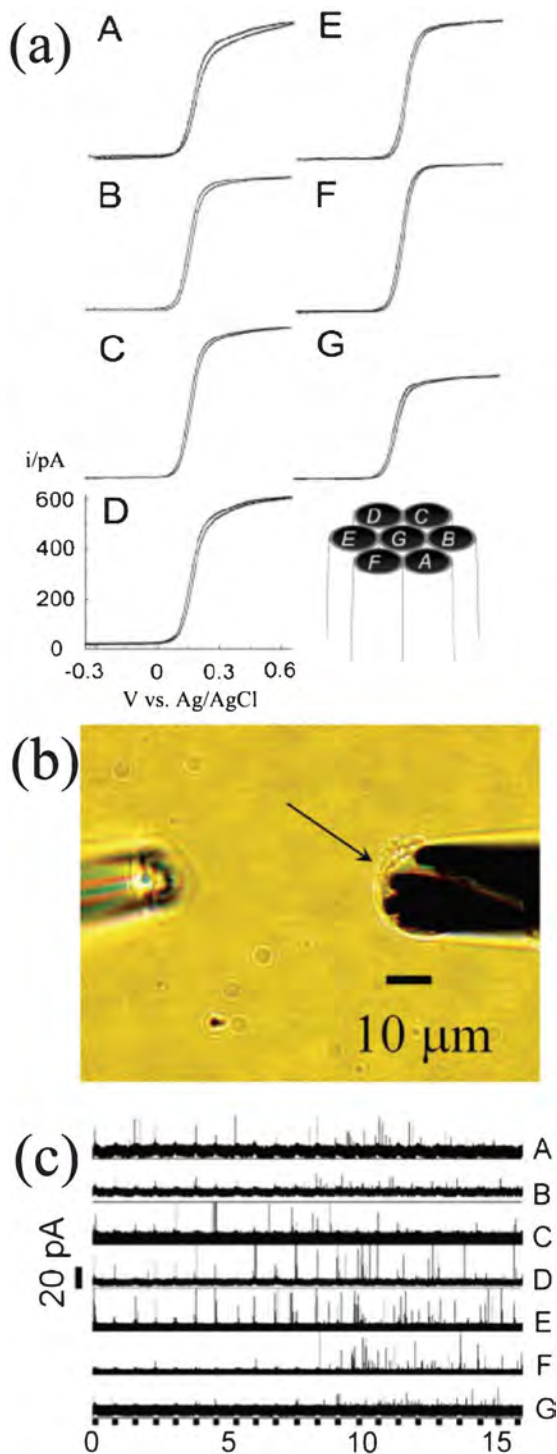
Fig. 10 (a) Steady-state voltammetric response at 20 mV s^{-1} of a seven-fiber MEA in 1 mM FcCH$_2$OH and 0.2 M KCl. (A)–(G) are the voltammetric response of individual microelectrodes A–G as shown in the schematic of the microelectrode assemble shows in the bottom right. (b) Optical image showing a microelectrode array positioned over a single PC12 cell (right) and a stimulation pipet (left). The cell is denoted with an arrow. (c) Amperometric traces of exocytotic release from a PC12 cell recorded using a microelectrode array. Thick black lines along the time axis indicate exposure to high potassium stimuli (100 mM, 5 s pulse every 45 s). Reprinted with permission from ref. 101, copyright 2008 American Chemical Society.

4. Application in electrochemical sensors

4.1 Functionalization of carbon microelectrodes

Functionalization of VACNFs is a critical component in the applications of these high aspect ratio structures to practical devices. Photoresist blocking strategies are developed for site-specific physical, chemical, and electrochemical functionalization of nanofiber arrays both spatially across regions of the device as well as along the length of the vertical nanofibers.[103] These approaches are explored for the functionalization of CNFs surfaces with gold, conductive polymers, and DNA and for biotinylation and subsequent capture of active enzyme- and quantum-dot-conjugated (strept)avidins. The redox-active protein cytochrome *c* can be immobilized on VACNFs by carboxylic acid group functionalization, which shows effective binding cytochrome *c* to CNFs.[28] The nanofiber-bound protein presents well-defined CV peaks. VACNFs modified with cytochrome *c* yield approximately 10 times higher activity than similarly modified surfaces of GC and gold. However, cytochrome *c* modified nanofibers also yield a high capacitive background thus reducing the signal to noise ratio of the electrical measurements. The high capacitive current may be partly due to inhomogeneous functionalization of the nanofibers at edge-plane *versus* basal-plane sites on the nanofiber surface, leading to leaky monolayers that yield increased capacitance. The vertical orientation of VACNFs presents edge-plane sites along the sidewalls that provide desirable electrochemical properties. By using a model organosilicon electrolyte solution, the resulting interfaces yield interfacial capacitances equal to the increase in geometric area, indicating full electrochemical accessibility of the nanofiber side-walls.[104] Measurements as a function of potential show perfect stability at applied voltages up to 3 V. The results are beneficial to the understanding of the ability to integrate organosilicon electrolytes with high-surface-area carbon materials in electrochemical applications.

The ET properties of redox-active molecules covalently linked to the surface of VACNFs are investigated by the ferrocene model.[105] Ultraviolet grafting of organic alkenes is used to prepare carboxylic acid-terminated layers and ferrocene is then linked to these layers *via* amide groups, as shown in Fig. 11a–b. No significant changes are observed from the electron-transfer rate constants upon different molecular layer lengths as well as dilution of the ferrocene-containing molecules, because molecular layers grafted to carbon nanofibers are sparse and disordered compared to those commonly studied on planar surfaces. This behavior is quite distinct from the more commonly observed CNTs, which present edge-plane sites only at the ends. A form of "click" chemistry is employed to covalently link ferrocene groups to VACNFs *via* the Cu(I)-catalyzed azide alkyne cycloaddition (CuAAC).[106] The VACNFs are terminated with azide groups followed by attachment of ethynylferrocene through a 1,4-disubstituted 1,2,3-triazole linkage (Fig. 11c–d). It provides fast and highly stable attachment of electrochemically active ferrocene groups to the nanofibers. The rates of electron transfer are found to be slightly larger than those measured through alkyl linkages to the VACNF surface. Stability tests
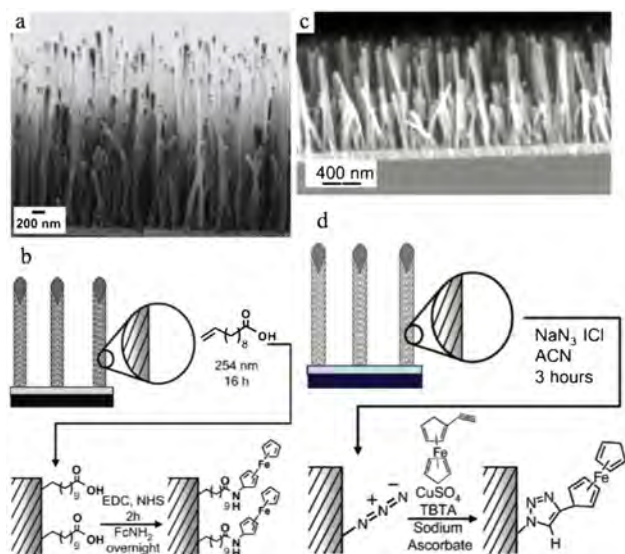
Fig. 11 (a) SEM image of the as-grown VACNF surfaces, (b) reaction scheme of the ferrocene attachment to the VACNF surface, (c) SEM image of vertically aligned carbon nanofiber crosssection, (d) reaction scheme of ferrocene attachment to the VACNF surface. (a) and (b) Reprinted with permission from ref. 105, copyright 2008 American Chemical Society. (c) and (d) Reprinted with permission from ref. 106, copyright 2009 American Chemical Society.

show that the covalently grafted ferrocene groups are stable for more than 1500 repeated cyclic voltammograms and over a potential window of >1.5 V limited by the solvent. Functionalization of VACNFs with 1-alkenes using ultraviolet light is investigated as a potential way to impart a variety of different functional groups onto the nanofiber sidewalls.[29] The impact of nanofiber growth rate on both the amount of exposed edge-plane sites and the resulting electrochemical activity toward $Ru(NH_3)_6^{3+/2+}$ and $Fe(CN)_6^{3-/4-}$ redox couples is explored. The surface oxides are unaffected by the grafting of alkenes to the nanofibers. The edge plane sites are preferred sites for photochemical grafting, but grafting of molecular layers only slightly reduces the overall electrochemical activity of the nanofibers due to the reduction of the available redox-active area. The overall Fermi-level density of states of the nanofibers is not significantly impacted by photochemical functionalization. The amount of exposed edge-plane sites depends on the nanofiber growth rate, with the slowest growth showing the largest angle and therefore leading to the smallest separation between edge-plane sites. By varying the nanofiber growth conditions, it is possible to tune the amount of edge-plane sites and thereby control the ratio of edge-plane to basal-plane sites. This connection between the surface structure and chemical reactivity indicates that chemical functionalization of the surfaces can be controlled by chemical means and the underlying surface structure. The results provide new insights to the relationships between the chemical reactivity and electrochemical properties of nanostructured carbon materials and highlight the crucial role that exposed edge-plane sites play in the electrochemical properties of CNTs and CNFs.

4.2 Enzymatic sensors and immunosensors

Besides facilitating the heterogeneous electron-transfer process of electrochemical reaction, the edge plane sites on carbon nanomaterials are readily bonded to enzymes or antibodies for selective and sensitive biosensing. The aligned CNTs are covalently attached to Au electrodes by self-assembly, followed by immobilization of HRP onto the tube ends of CNTs.[12] Enzyme catalyzed H_2O_2 then induces deposition of polyaniline (PANI) on the CNT arrays in the presence of H_2O_2 and aniline. Compared to other electropolymerized PANI sensors, the sensitivity of the PANI/HRP/CNTs sensor is increased by three orders of magnitude that may be ascribed to the orderly arrangement of CNTs and highly efficient polymerization of PANI in the enzymatic reaction. A sandwiched immunoassay consisting of HRP conjugated to a secondary antibody and/or a polymer bead loaded with multi-enzyme labels has been demonstrated in the detection of a cancer biomarker protein matrix metalloproteinase-3 (MMP-3) based on VACNTs.[107] The detection limit is 0.4 ng mL^{-1} (7.7 pM) for the 14–16 label sensor protocol and 4 pg mL^{-1} (77 fM) using a multiply enzyme labeled polymeric bead amplification strategy in 10 μL of calf serum. Some examples of enzymatic sensors and immunosensors based on CNT or CNF arrays are listed in Table 1.

Table 1 Examples of enzymatic sensors and immunosensors based on carbon-related MEAs

MEAs arrangement	Sensing elements	Target analytes	Reference
VACNTs	glucose oxidase	glucose	108
VACNTs	glucose oxidase	glucose	109
VACNTs	hemoglobin	H_2O_2	110
VACNTs	cholesterol enzymes	cholesterol	111
VACNTs	glutamate dehydrogenase	glutamate	30
VACNTs	Anti-mouse IgG	mouse IgG	73
VACNTs	anti-MMP-3/HRP	MMP-3	107
self-assembly CNTs	flavin adenine dinucleotide/glucose oxidase	glucose	85
self-assembly CNTs	PANI/HRP	H_2O_2	12
self-assembly CNTs	biotin/anti-biotin IgG	anti-biotin	112
self-assembly CNTs	anti-endosulfan IgG	endosulfan	88
low density CNTs	glucose oxidase	glucose	95
VACNFs	yeast alcohol dehydrogenase	ethanol	113
VACNFs	ricin-A antibody/ricin aptamer	ricin	114

Table 2 Carbon-based MEAs for the determination of small organic and inorganic ions

MEAs arrangement	Sensing elements	Target analytes	Reference
VACNTs	Co catalysts residue	glucose	115
VACNTs	Pt nanoparticles	glucose	116
VACNTs	MnO_2	glucose	117
VACNTs	Cu nanoparticles	glucose	118
VACNTs	Cu nanocubes	glucose	119
VACNTs	copper oxide nanoparticles	glucose	120
VACNTs		UA, AA	64
VACNTs	RuO_2	DA	121
VACNTs		guanine, adenine	122
VACNTs		salicylic acid	54
VACNTs	Pt nanoparticles	L-cysteine	66
VACNTs	thionine	nitrite	123
VACNTs	TiO_2 nanoparticles	H_2O_2	124
VACNTs		Pb^{2+}, Cd^{2+}, Cu^{2+} and Zn^{2+}	125
VACNTs		glutathione	126
self-assembly CNTs	octa(hydroxyethylthio)-phthalocyaninatoiron(II)	pH	87
low-density CNTs		Pb^{2+}, Cd^{2+}	10
low-density CNTs		Pb^{2+}	96
core–shell CNFs		AA, DA, and UA	57
core–shell CNFs		AA, UA	27
core–shell CNFs		hydrazine	62

4.3 Determination of small organic and inorganic ions

Carbon-based MEAs have been extensively explored for the determination of a variety of small organic and inorganic ions such as glucose, UA, DA, AA, guanine, adenine, nitrite, H_2O_2, and heavy metal ions due to the advantages offered by both carbon nanomaterials and MEAs. Favorable voltammetric and amperometric responses are acquired directly from the carbon-based MEAs or the modified MEAs, suggesting a promising prospect of these electrochemical sensors. Some important applications are summarized in Table 2 that gives a general view of the recent developments.

5. Conclusions

Carbon nanomaterials have become an essential component in electrochemical sensors. Because of the various advantages, carbon-based MEAs, especially aligned CNTs, and CNFs, have been extensively explored to determine the amounts of analytes including neurotransmitters, proteins, pesticides, glucose, and heavy metal ions, in biological and environmental samples. The edge planes on carbon nanomaterials are electrochemically active as well as chemically active. These properties are fundamental to the understanding of the electrochemistry and/or chemistry of carbon nanomaterials. PECVD and self-assembly are frequently employed to prepare aligned CNTs and/or CNFs with a large specific surface area. However, the voltammograms of closely packed MEAs are similar to those of a macroelectrode due to the substantial overlap of the diffusion layer. By coupling highly orientated synthesis with catalyst patterning techniques such as photolithography and controllable electrodeposition, carbon-based MEAs can be synthesized at precisely defined locations. Low-density CNTs and individually addressable CNFs can be produced for fast establishment of a steady-state and multi-mode recordings at high spatial resolution. By introducing a nanowire core along the axis of CNFs to facilitate electron transfer, core–shell TiO_2/C and TiC/C nanofiber arrays are prepared on Ti or Ti alloyed substrates *via* catalyst-free methods that do not require a foreign metallic catalyst or template. The TiC/C nanofibers exhibit extremely high heterogeneous charge transfer rates which can be ascribed to their good electrical contact as well as the highly conducting TiC nanowire core that offers an ideal transport pathway for electrons.

Continuous and vigorous development pertaining to the design and construction of high performance and low cost carbon-based MEAs is expected and so are results yielding practical applications. For example, micro- and nanolithography is currently limited to being a research technique due to the expensive instruments and high maintenance cost. The advent of higher resolution conventional photolithographic techniques and high-throughput patterning technologies will make it possible to turn this process into a large scale production technology.

Acknowledgements

References

1 A. J. Bard and L. R. Faulkner, *Electrochemical Methods: Fundamentals and Applications*, 2nd ed., John Wiley & Sons, Inc., New York, 2001, pp. 156–225.

2 R. M. Wightman, *Anal. Chem.*, 1981, **53**, 1125A.

3 S. Pons and M. Fleischman, *Anal. Chem.*, 1987, **59**, 1391A.

4 A. C. Michael and R. M. Wightman, *Laboratory Techniques in Electroanalytical Chemistry*, P. T. Kissinger and W. R. Heineman, ed., Marcel Dekker, New York, 1996, pp. 367–403.

5 R. M. Wightman, *Science*, 2006, **311**, 1570.

6 W. Kutner, *Pure Appl. Chem.*, 2000, **72**, 1483.

7 A. Yakushenko, J. Schnitker and B. Wolfrum, *Anal. Chem.*, 2012, **84**, 4613.

8 T. E. Mcknight, A. V. Melechko, B. L. Fletcher, S. W. Jones, D. K. Hensley, D. B. Peckys, G. D. Griffin, M. L. Simpson and M. N. Ericson, *J. Phys. Chem. B*, 2006, **110**, 15317.

9 B. A. Patel, M. Arundell, I. R. Ellis, M. M. Florence, A. E. G. Cass, A. M. Schor and D. O. Hare, *Anal. Bioanal. Chem.*, 2008, **390**, 1379.

10 G. D. Liu, Y. H. Lin, Y. Tu and Z. F. Ren, *Analyst*, 2005, **130**, 1098.

11 P. U. Arumugam, E. Yu, R. Riviere and M. Meyyappan, *Chem. Phys. Lett.*, 2010, **499**, 241.

12 N. Tang, J. B. Zheng, Q. L. Sheng, H. F. Zhang and R. X. Liu, *Analyst*, 2011, **136**, 781.

13 X. J. Huang, A. M. O'Mahony and R. G. Compton, *Small*, 2009, **5**, 776.

14 R. L. McCreery and K. K. Cline, *Laboratory Techniques in Electroanalytical Chemistry*, P. T. Kissinger and W. R. Heineman, ed., Marcel Dekker, New York, 1996, pp. 293–332.

15 R. L. McCreery, *Chem. Rev.*, 2008, **108**, 2646.

16 C. E. Banks, T. J. Davies, G. G. Wildgoose and R. G. Compton, *Chem. Commun.*, 2005, 829.

17 A. V. Melechko, V. I. Merkulov, T. E. McKnight, M. A. Guillorn, K. L. Klein, D. H. Lowndes and M. L. Simpson, *J. Appl. Phys.*, 2005, **97**, 041301.

18 C. Rao, A. K. Sood, K. S. Subrahmanyam and A. Govindaraj, *Angew. Chem., Int. Ed.*, 2009, **48**, 7752.

19 A. V. Melechko, K. L. Klein, J. D. Fowlkes, D. K. Hensley, I. A. Merkulov, T. E. McKnight, P. D. Rack, J. A. Horton and M. L. Simpson, *J. Appl. Phys.*, 2007, **102**, 074314.

20 A. Ambrosi, T. Sasaki and M. Pumera, *Chem.–Asian J.*, 2010, **5**, 266.

21 R. S. Chen, W. H. Huang, H. Tong, Z. L. Wang and J. K. Cheng, *Anal. Chem.*, 2003, **75**, 6341.

22 Q. J. Wan, H. Cai, Y. Liu, H. T. Song, H. L. Liao, S. T. Liu and N. J. Yang, *Chem.–Eur. J.*, 2013, **19**, 3483.

23 H. C. Chen, Y. H. Chen, S. L. Chen, Y. T. Chern, R. Y. Tsai and M. Y Hua, *Biosens. Bioelectron.*, 2013, **46**, 84.

24 N. G. Shang, P. Papakonstantinou, M. McMullan, M. Chu, A. Stamboulis, A. Potenza, S. S. Dhesi and H. Marchetto, *Adv. Funct. Mater.*, 2008, **18**, 3506.

25 P. Li, Y. Ding, A. Wang, L. Zhou, S. H. Wei, Y. M. Zhou, Y. W. Tang, Y. Chen, C. X. Cai and T. H. Lu, *ACS Appl. Mater. Interfaces*, 2013, **5**, 2255.

26 A. Ambrosi and M. Pumera, *Phys. Chem. Chem. Phys.*, 2010, **12**, 8943.

27 R. S. Chen, L. S. Hu, K. F. Huo, J. J. Fu, H. W. Ni, Y. Tang and P. K. Chu, *Chem.–Eur. J.*, 2011, **17**, 14552.

28 S. E. Baker, P. E. Colavita, K. Tse and R. J. Hamers, *Chem. Mater.*, 2006, **18**, 4415.

29 E. C. Landis, K. L. Klein, A. Liao, E. Pop, D. K. Hensley, A. V. Melechko and R. J. Hamers, *Chem. Mater.*, 2010, **22**, 2357.

30 G. Azam, S. Saeed, I. Z. Azam, M. Shamsoddin, V. Manouchehr, D. Sara and S. Zeinab, *Biosens. Bioelectron.*, 2012, **31**, 110.

31 S. Musa, D. R. Rand, D. J. Cott, J. Loo, C. Bartic, W. Eberle, B. Nuttin and G. Borghs, *ACS Nano*, 2012, **6**, 4615.

32 X. M. Liu, K. H. R. Baronian and J. D. Alison, *Anal. Chem.*, 2008, **80**, 8835.

33 M. A. Guillorn, T. E. McKnight, A. Melechko, V. I. Merkulov, P. F. Britt, D. W. Austin, D. H. Lowndes and M. L. Simpson, *J. Appl. Phys.*, 2002, **91**, 3824.

34 B. L. Fletcher, T. E. McKnight, A. V. Melechko, D. K. Hensley, D. K. Thomas, M. N. Ericson and M. L. Simpson, *Adv. Mater.*, 2006, **18**, 1689.

35 S. Siddiqui, P. U. Arumugam, H. Chen, J. Li and M. Meyyappan, *ACS Nano*, 2010, **4**, 955.

36 A. F. M. Johnstone, G. W. Gross, D. G. Weiss, O. H. U. Schroeder, A. Gramowski and T. J. Shafer, *NeuroToxicology*, 2010, **31**, 331.

37 P. M. Ajayan, *Chem. Rev.*, 1999, **99**, 1787.

38 X. S. Wang, Q. Q. Li, J. Xie, Z. Jin, J. Y. Wang, Y. Li, K. L. Jiang and S. S. Fan, *Nano Lett.*, 2009, **9**, 3137.

39 M. Pumera, A. Merkoçi and S. Alegret, *Sens. Actuators, B*, 2006, **113**, 617.

40 A. G. Crevillén, M. Ávila, M. Pumera, M. C. González and A. Escarpa, *Anal. Chem.*, 2007, **79**, 7408.

41 S. N. Kim, J. F. Rusling and F. Papadimitrakopoulos, *Adv. Mater.*, 2007, **19**, 3214.

42 J. J. Gooding, R. Wibowo, J. Q. Liu, W. R. Yang, D. Losic, S. Orbons, F. J. Mearns, J. G. Shapter and D. B. Hibbert, *J. Am. Chem. Soc.*, 2003, **125**, 9006.

43 C. E. Banks, R. R. Moore, T. J. Davies and R. G. Compton, *Chem. Commun.*, 2004, 1804.

44 J. M. Nugent, K. S. V. Santhanam, A. Rubio and P. M. Ajayan, *Nano Lett.*, 2001, **1**, 87.

45 K. P. Gong, S. Chakrabarti and L. M. Dai, *Angew. Chem.*, 2008, **120**, 5526.

46 M. Pumera, T. Sasaki and H. Iwai, *Chem.–Asian J.*, 2008, **3**, 2046.

47 V. Vamvakaki, K. Tsagaraki and N. Chaniotakis, *Anal. Chem.*, 2006, **78**, 5538.

48 S. J. Randolph, J. D. Fowlkes, A. V. Melechko, K. L. Klein, H. M. Meyer III and M. L. Simpson, *Nanotechnology*, 2007, **18**, 465304.

49 K. D. Sorge, K. L. Klein, A. V. Melechko, C. L. Finkel, O. Malkina, T. Leventouri, J. D. Fowlkes, P. D. Rack and M. L. Simpson, *J. Appl. Phys.*, 2008, **104**, 033909.

50 R. Longtin, C. Fauteux, L. P. Carignan, D. Therriault and J. Pegna, *Surf. Coat. Technol.*, 2008, **202**, 2661.

51 R. C. Pearce, A. V. Vasenkov, D. K. Hensley, M. L. Simpson, T. E. McKnight and A. V. Melechko, *ACS Appl. Mater. Interfaces*, 2011, **3**, 3501.

52 Y. D. Li, D. X. Li and G. W. Wang, *Catal. Today*, 2011, **162**, 1.

53 K. L. Klein, A. V. Melechko, T. E. McKnight, S. T. Retterer, P. D. Rack, J. D. Fowlkes, D. C. Joy and M. L. Simpson, *J. Appl. Phys.*, 2008, **103**, 061301.

54 W. D. Zhang, B. Xu, Y. X. Hong, Y. X. Yu, J. S. Ye and J. Q. Zhang, *J. Solid State Electrochem.*, 2010, **14**, 1713.

55 J. Zhang, X. Wang, W. Yang, W. Yu, T. Feng, Q. Li, X. Liu and C. Yang, *Carbon*, 2006, **44**, 418.

56 Y. Matsuda, W. Q. Deng and W. A. Goddard, *J. Phys. Chem. C*, 2007, **111**, 11113.

57 L. S. Hu, K. F. Huo, R. S. Chen, X. M. Zhang, J. J. Fu and P. K. Chu, *Chem. Commun.*, 2010, **46**, 6828.

58 L. Z. Zhao, L. S. Hu, K. F. Huo, Y. M. Zhang, Z. F. Wu and P. K. Chu, *Biomaterials*, 2010, **31**, 8341.

59 K. F. Huo, X. M. Zhang, L. S. Hu, X. J. Sun, J. J. Fu and P. K. Chu, *Appl. Phys. Lett.*, 2008, **93**, 013105.

60 R. S. Chen, L. S. Hu, X. M. Zhang, J. J. Fu, K. F. Huo, P. K. Chu and J. K. Cheng, *Chem. J. Chinese U.*, 2008, **29**, 2542.

61 X. M. Zhang, K. F. Huo, H. R. Wang, B. Gao, J. J. Fu, T. F. Hung and P. K. Chu, *ACS Appl. Mater. Interfaces*, 2012, **4**, 1037.

62 W. R. Zhang, K. F. Huo, Y. L. Jiang, L. S. Hu, R. S. Chen and P. K. Chu, *Microchim. Acta*, 2011, **175**, 137.

63 L. M. Li, X. Y. Wang, L. S. Hu, R. S. Chen, Y. Huang, S. J. Chen, W. H. Huang, K. F. Huo and P. K. Chu, *Lab Chip*, 2012, **12**, 4249.

64 J. S. Ye, Y. Wen, W. D. Zhang, M. Gan, Q. Xu and F. S. Sheu, *Electroanalysis*, 2003, **15**, 1693.

65 H. Y. Yeo, Y. D. Zhong, N. S. Vesselin, D. Amos, R. H. William, H. B. Halsall, B. Amit, K. Y. W. Danny and J. S. Mark, *Sens. Actuators, B*, 2008, **133**, 208.

66 M. L. Ye, B. Xu and W. D. Zhang, *Microchim. Acta*, 2011, **172**, 439.

67 T. J. Davies, C. E. Banks and R. G. Compton, *J. Solid State Electrochem.*, 2005, **9**, 797.

68 C. E. Banks, A. Crossley, C. Salter, S. J. Wilkins and R. G. Compton, *Angew. Chem., Int. Ed.*, 2006, **45**, 2533.

69 Š. Biljana, E. B. Craig and G. C. Richard, *Nano Lett.*, 2006, **6**, 1556.

70 M. Pumera and Y. Miyahara, *Nanoscale*, 2009, **1**, 260.

71 F. Javier del Campo, J. García-Céspedes, F. X. Muñoz and E. Bertrán, *Electrochem. Commun.*, 2008, **10**, 1242.

72 H. Y. Yeo, S. Vesselin, J. S. Mark, Y. D. Zhong, J. Abdul, R. H. William, H. B. Halsall, K. Y. Danny, A. B. Wong, T. Yi and S. Srinivas, *Sens. Actuators, B*, 2006, **120**, 298.

73 H. Y. Yeo, B. Adam, R. H. William, H. B. Halsall, N. S. Vesselin, Y. D. Zhong, P. Sarah, B. Michael, J. Abdul, T. Yi, K. Y. Danny, A. B. Wong and J. S. Mark, *Sens. Actuators, B*, 2007, **123**, 177.

74 D. J. Garrett, P. A. Brooksby, F. J. Rawson, K. H. R. Baronian and A. J. Downard, *Anal. Chem.*, 2011, **83**, 8347.

75 T. E. McKnight, A. V. Melechko, M. A. Guillorn, V. I. Merkulov, M. J. Doktycz, C. T. Culbertson, S. C. Jacobson, D. H. Lowndes and M. L. Simpson, *J. Phys. Chem. B*, 2003, **107**, 10722.

76 M. Endo, Y. A. Kim, T. Hayashi, Y. Fukai and K. Oshida, *Appl. Phys. Lett.*, 2002, **80**, 1267.

77 M. Pumera, *Langmuir*, 2007, **23**, 6453.

78 T. Kolodiazhnyi and M. Pumera, *Small*, 2008, **4**, 1476.

79 C. T. Lin, W. C. Chen, M. Y. Yen, L. S. Wang, C. Y. Lee, T. S. Chin and H. T. Chiu, *Carbon*, 2007, **45**, 411.

80 K. X. Wang, W. H. Zhang, R. Phelan, M. A. Morris and J. D. Holmes, *J. Am. Chem. Soc.*, 2007, **129**, 13388.

81 A. C. M. S. Dias, S. L. R. Gomes-Filho, M. M. S. Silva and R. F. Dutra, *Biosens. Bioelectron.*, 2013, **44**, 216.

82 R. Akter, M. A. Rahman and C. K. Rhee, *Anal. Chem.*, 2012, **84**, 6407.

83 P. Diao and Z. F. Liu, *J. Phys. Chem. B*, 2005, **109**, 20906.

84 A. Chou, T. Bocking, N. K. Singh and J. J. Gooding, *Chem. Commun.*, 2005, 842.

85 J. Q. Liu, A. Chou, W. Rahmat, N. P. R. Michael and J. J. Gooding, *Electroanalysis*, 2005, **17**, 38.

86 J. J. Gooding, A. Chou, J. Q. Liu, D. Losic, J. G. Shapter and D. B. Hibbert, *Electrochem. Commun.*, 2007, **9**, 1677.

87 D. Nkosi and K. I. Ozoemena, *Electrochim. Acta*, 2008, **53**, 2782.

88 G. Z. Liu, S. Wang, J. Q. Liu and D. D. Song, *Anal. Chem.*, 2012, **84**, 3921.

89 G. Z. Liu, T. Bocking and J. J. Gooding, *J. Electroanal. Chem.*, 2007, **600**, 335.

90 S. J. Hood, D. K. Kampouris, R. O. Kadara, N. Jenkinson, F. Javier del Campo, F. X. Muñoz and C. E. Banks, *Analyst*, 2009, **134**, 2301.

91 J. Li, H. T. Ng, A. M. Cassell, W. Fan, H. Chen, Q. Ye, J. Koehne, J. Han and M. Meyyappan, *Nano Lett.*, 2003, **3**, 597.

92 J. Koehne, J. Li, A. M. Cassell, H. Chen, Q. Ye, H. T. Ng, J. Han and M. Meyyappan, *J. Mater. Chem.*, 2004, **14**, 676.

93 Y. Tu, Z. P. Huang, D. Z. Wang, J. G. Wen and Z. F. Ren, *Appl. Phys. Lett.*, 2002, **80**, 4018.

94 Y. Tu, Y. H. Lin and Z. F. Ren, *Nano Lett.*, 2003, **3**, 107.

95 Y. H. Lin, F. Lu, Y. Tu and Z. F. Ren, *Nano Lett.*, 2004, **4**, 191.

96 Y. Tu, Y. H. Lin, W. Yantasee and Z. F. Ren, *Electroanalysis*, 2005, **17**, 79.

97 T. E. McKnight, A. V. Melechko, D. W. Austin, T. Sims, M. A. Guillorn and M. L. Simpson, *J. Phys. Chem. B*, 2004, **108**, 7115.

98 C. S. Lee, S. E. Baker, M. S. Marcus, W. S. Yang, M. A. Eriksson and R. J. Hamers, *Nano Lett.*, 2004, **4**, 1713.

99 Z. Yu, T. E. McKnight, M. N. Ericson, A. V. Melechko, M. L. Simpson and B. Morrison, *Nano Lett.*, 2007, **7**, 2188.

100 P. U. Arumugam, H. Chen, S. Siddiqui, J. A. P. Weinrich, A. Jejelowo, J. Li and M. Meyyappan, *Biosens. Bioelectron.*, 2009, **24**, 2818.

101 B. Zhang, L. A. Kelly, J. L. Sarah, J. E. Daniel, L. H. Michael and G. E. Andrew, *Anal. Chem.*, 2008, **80**, 1394.

102 B. Zhang, L. A. Michael, V. Heien, F. S. Michael, M. Lisa and G. E. Andrew, *Anal. Chem.*, 2011, **83**, 571.

103 T. E. Mcknight, C. Peeraphatdit, S. W. Jones, J. D. Fowlkes, B. L. Letcher, K. L. Klein, A. V. Melechko, M. J. Doktycz and M. L. Simpson, *Chem. Mater.*, 2006, **18**, 3203.

104 K. Y. Tse, L. Z. Zhang, S. E. Baker, B. M. Nichols, R. West and R. J. Hamers, *Chem. Mater.*, 2007, **19**, 5734.

105 E. C. Landis and R. J. Hamers, *J. Phys. Chem. C*, 2008, **112**, 16910.

106 E. C. Landis and R. J. Hamers, *Chem. Mater.*, 2009, **21**, 724.

107 B. S. Munge, J. Fisher, L. N. Millord, C. E. Krause, R. S. Dowd and J. F. Rusling, *Analyst*, 2010, **135**, 1345.

108 M. Gao, L. M. Dai and G. G. Wallace, *Electroanalysis*, 2003, **15**, 1089.

109 S. Sotiropoulou and N. A. Chaniotakis, *Anal. Bioanal. Chem.*, 2003, **375**, 103.

110 J. Yang, Y. Xu, R. Y. Zhang, Y. Z. Wang, P. G. He and Y. Z. Fang, *Electroanalysis*, 2009, **21**, 1672.

111 A. Wisitsoraat, C. Karuwan, K. Wong-ek, D. Phokharatkul, P. Sritongkham and A. Tuantranont, *Sensors*, 2009, **9**, 8658.

112 G. Z. Liu and J. J. Gooding, *Electrochem. Commun.*, 2009, **11**, 1982.

113 M. L. Weeks, T. Rahman, P. D. Frymier, S. K. Islam and T. E. McKnight, *Sens. Actuators, B*, 2008, **133**, 53.

114 A. Periyakaruppan, P. U. Arumugam, M. Meyyappan and J. E. Koehne, *Biosens. Bioelectron.*, 2011, **28**, 428.

115 J. S. Ye, Y. Wen, W. D. Zhang, L. M. Gan, G. Q. Xu and F. S. Sheu, *Electrochem. Commun.*, 2004, **6**, 66.

116 K. Zhao, S. Q. Zhuang, Z. Chang, H. Y. Songm, L. M. Dai, P. G. He and Y. Z. Fang, *Electroanalysis*, 2007, **19**, 1069.

117 J. Chen, W. D. Zhang and J. S. Ye, *Electrochem. Commun.*, 2008, **10**, 1268.

118 J. Yang, L. C. Jiang, W. D. Zhang and S. Gunasekaran, *Talanta*, 2010, **82**, 25.

119 J. Yang, W. D. Zhang and S. Gunasekaran, *Biosens. Bioelectron.*, 2010, **26**, 279.

120 F. Jiang, S. Wang, J. J. Lin, H. L. Jin, L. J. Zhang, S. M. Huang and J. C. Wang, *Electrochem. Commun.*, 2011, **13**, 363.

121 L. C. Jiang and W. D. Zhang, *Electroanalysis*, 2009, **21**, 1811.

122 F. Berti, L. Lozzi, I. Palchetti, S. Santucci and G. Marrazza, *Electrochim. Acta*, 2009, **54**, 5035.

123 K. Zhao, H. Y. Song, S. Q. Zhuang, L. M. Dai, P. G. He and Y. Z. Fang, *Electrochem. Commun.*, 2007, **9**, 65.

124 L. C. Jiang and W. D. Zhang, *Electroanalysis*, 2009, **21**, 988.

125 X. F. Guo, Y. Yeoheung, N. Vesselin, H. Shanov, H. Brian and R. H. William, *Electroanalysis*, 2011, **23**, 1252.

126 H. Tang, J. H. Chen, L. H. Nie, S. Z. Yao and Y. F. Kuang, *Electrochim. Acta*, 2006, **51**, 3046.